AD-A077 902 ENVIRONMENTAL RESEARCH AND TECHNOLOGY INC CONCORD MA F/G 4/2
COMPARATIVE STUDY OF ANOMALOUS GRAY-SHADE PATTERNS IN DMSP AND --ETC(U)
SEP 79 J C BARNES , C J BOWLEY , R G ISAACS N00228-77-C-3164
UNCLASSIFIED ERT-P-3469 NEPRF-CR-79-05 NL

1 OF 2
AD
A077902

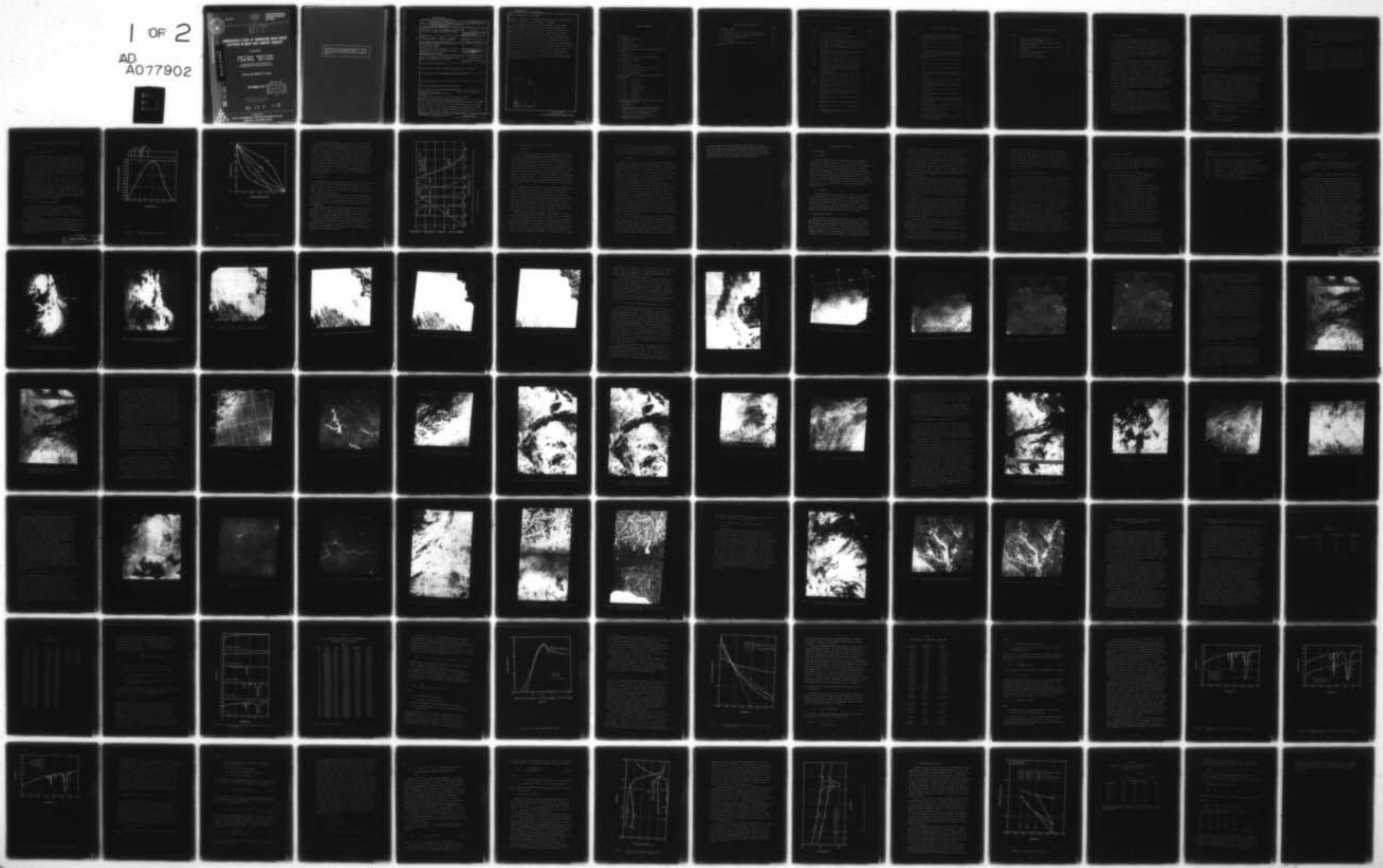

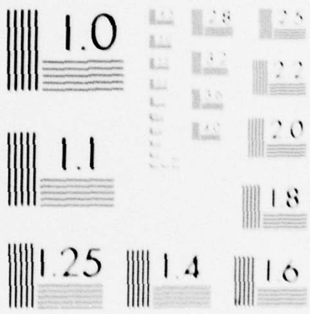

MICROCOPY RESOLUTION TEST CHART

NATIONAL BUREAU OF STANDARDS 1963-A

ERT P-3469

82

NAVENVPREDRSCHFAC
CONTRACTOR REPORT
CR 79-05

LEVEL II

NAVENVPREDRSCHFAC CR 79-05

COMPARATIVE STUDY OF ANOMALOUS GRAY-SHADE PATTERNS IN DMSP AND LANDSAT IMAGERY

Prepared By:

James C. Barnes   Ronald G. Isaacs
C. James Bowley   Allen J. Bussey

Environmental Research & Technology, Inc.
696 Virginia Road, Concrd, Massachusetts 01742

Contract No. N00228-77-C-3164

SEPTEMBER 1979

APPROVED FOR PUBLIC RELEASE
DISTRIBUTION UNLIMITED

Prepared For:
NAVAL ENVIRONMENTAL PREDICTION RESEARCH FACILITY
MONTEREY, CALIFORNIA 93940

REPORT DOCUMENTATION PAGE

READ INSTRUCTIONS BEFORE COMPLETING FORM

1. REPORT NUMBER (19) NAVENVPREDRSCHFAC Contractor ~~Report~~ CR 79-05

2. GOVT ACCESSION NO. (18) NEPRF

3. RECIPIENT'S CATALOG NUMBER

4. TITLE (and Subtitle) (6) Comparative Study of Anomalous Gray-Shade Patterns in DMSP and LANDSAT Imagery.

5. TYPE OF REPORT & PERIOD COVERED (9) Final rept.

6. PERFORMING ORG. REPORT NUMBER (14) ERT-P-3469

7. AUTHOR(s) (10)
James C. Barnes, Ronald G. Isaacs
C. James Bowley, Allen J. Bussey

8. CONTRACT OR GRANT NUMBER(s) (15) N00228-77-C-3164

9. PERFORMING ORGANIZATION NAME AND ADDRESS
Environmental Research & Technology, Inc.
696 Virginia Road
Concord, MA 01742

10. PROGRAM ELEMENT, PROJECT, TASK AREA & WORK UNIT NUMBERS (12) 104

11. CONTROLLING OFFICE NAME AND ADDRESS
Commander, Naval Air Systems Command
Department of the Navy
Washington, DC 20361

12. REPORT DATE (11) Sept~~ember~~ 1979

13. NUMBER OF PAGES 108

14. MONITORING AGENCY NAME & ADDRESS (if different from Controlling Office)
Naval Environmental Prediction Research
Facility, Monterey, CA 93940

15. SECURITY CLASS. (of this report) UNCLASSIFIED

15a. DECLASSIFICATION/DOWNGRADING SCHEDULE

16. DISTRIBUTION STATEMENT (of this Report)

Approved for public release; distribution unlimited.

17. DISTRIBUTION STATEMENT (of the abstract entered in Block 20, if different from Report)

18. SUPPLEMENTARY NOTES

Original manuscript received April 1979.

19. KEY WORDS (Continue on reverse side if necessary and identify by block number)
Gray shade patterns
Anomalous gray-shade patterns
LANDSAT
Defense Meteorological Satellite Program (DMSP)
Water vapor absorption

20. ABSTRACT (Continue on reverse side if necessary and identify by block number)

A comparative analysis of anomalous gray-shade patterns is performed using Defense Meteorological Satellite Program (DMSP) and Landsat multispectral imagery. Eight cases are analyzed where anomalous gray-shade patterns associated with reduced visibilities in light fog or haze are detected in DMSP imagery, and where corresponding Landsat data are → over

391 776 sut

(Block 20, Abstract, continued)

available. In addition, a detailed theoretical analysis of the effects of water vapor absorption on the imagery is performed.

The qualitative results of the imagery analysis indicate that within the anomalous gray-shade patterns as detected in the DMSP imagery, the Landsat MSS-4 (visible band) image will appear more hazy than the longer wavelength Landsat bands. The theoretical analysis indicates that simulated radiances from the DMSP are similar to the Landsat MSS-6 band, rather than to MSS-4. This apparent contradiction can be explained by considering the relative contributions of energy from the different spectral intervals comprising the total DMSP response rather than the response function alone; the different spatial resolutions of the DMSP and Landsat sensors may also be a factor. The results of the theoretical analysis further suggest that for realistic cases of high humidity and low visibility, it is the aerosol growth, not the growth in water vapor, that increases the radiance measured by the DMSP Very High Resolution (VHR) sensor.

TABLE OF CONTENTS

TABLE OF CONTENTS (Continued)

LIST OF ILLUSTRATIONS

LIST OF ILLUSTRATIONS (Continued)

LIST OF ILLUSTRATIONS (Continued)

1. INTRODUCTION

1.1 Purpose and Objectives

This study was performed for the Naval Environmental Prediction Research Facility by Environmental Research & Technology, Inc. (ERT). The purpose of the study is to compare Defense Meteorological Satellite Program (DMSP) and Landsat imagery in which anomalous gray-shade patterns associated with low visibility in light fog or haze can be detected. These low visibility situations are of tactical importance to the Navy since the obstructions to vision could have an impact on a variety of Naval weapons systems.

Anomalous gray-shade patterns associated with light fog and/or haze conditions and other features have been detected in the DMSP Very High Resolution (VHR) visible images. The spectral response of the DMSP visible channel is 0.4-1.1 micrometers (μm). The Landsat Multispectral Scanner System (MSS) has four spectral bands within the overall spectral response of the DMSP visible channel. It is possible, therefore, to compare the DMSP and Landsat multispectral images to determine the wavelengths where the anomalous gray-shade patterns are most pronounced. Through the comparative analysis of the imagery and a theoretical analysis of the effects of water vapor absorption in the near infrared, a better understanding can be gained of the type and size distribution of the scattering particles.

To satisfy the purpose of the study, the specific objectives were: (1) to analyze a minimum of 20 cases of DMSP data over marine and/or land areas where the reported visibility has been reduced to five nautical miles (nmi) or less in haze or light fog, and (2) to conduct a detailed theoretical analysis of water vapor absorption in the near infrared (beyond 0.7 μm) and its effects on the satellite imagery. The 20 cases also require that an anomalous gray-shade pattern be detectable in the DMSP image and that nearly concurrent (within two hours) Landsat data be available for the same area.

1.2 Data Sample

Early in the study it became apparent that a suitable data sample, consisting of at least 20 cases where all selection criteria were satisfied, would be difficult to assemble. A major problem limiting the amount of useful data is the infrequent repeat coverage and limited areal coverage of Landsat; Landsat images were often found to cover areas outside the anomalous gray-shade pattern seen in the concurrent DMSP image. Moreover, several potential cases were not usable because of poor quality DMSP or Landsat imagery.

As a result of the data collection difficulties, the data sample used in the study was not as extensive as had been originally hoped. However, with the assistance of the contract technical monitor, a sufficient number of cases with high quality DMSP images were collected to satisfy the contract requirements.

1.3 Theoretical Analysis

In this part of the study, a theoretical analysis was performed to describe in detail the influence of water vapor and haze on DMSP and Landsat satellite imagery. A radiative transfer computer algorithm was used to model the multiple scattering and absorption processes in a realistic atmosphere with a vertically inhomogeneous (varying) distribution of optically active species. A tropical model atmosphere was selected, and simulated satellite radiances (weighted by approximate spectral band passes) were computed over a wavelength range of 0.4-1.1 μm assuming a particular viewing geometry and a calm ocean background with a modeled surface reflectance. Four specific choices were made with respect to optical parameters of the atmosphere:

1) low humidity, clear atmosphere [0.034 grams (g) water vapor and 23 kilometers (km) visibility];
2) high humidity, hazy atmosphere (3.35 g water vapor and 5 km visibility);
3) low humidity, hazy atmosphere; and
4) high humidity, clear atmosphere.

The first two choices are probably physically realistic, while the second set helps delineate ranges of uncertainty. No attempt was made to include a consistent relative humidity/visibility relationship or parameterize humidity-dependent aerosol growth phenomenon.

1.4 Contents of Report

A further discussion of the detection of anomalous gray-shade patterns in DMSP visible images is given in Section 2 of the report. Section 2 also contains a description of the DMSP and Landsat sensor systems and data formats. The data search procedures and the resultant data sample are discussed in Section 3. The analysis of selected cases is presented in Section 4 and the theoretical analysis in Section 5. The results of the practical and theoretical analyses are discussed in Section 6. The conclusions and recommendations for further studies may be found in Section 7.

2. DESCRIPTION OF SATELLITE SYSTEMS AND DATA CHARACTERISTICS

2.1 DMSP Data

2.1.1 Sensor Characteristics

The DMSP data used in the study were from the Block 5C system. In particular, the data were those of the VHR radiameter visible channel measuring reflected solar radiation. This sensor has a nominal subpoint resolution of 0.3 nmi, although the actual resolution apparent in the imagery is a function of several factors. The VHR data swath is approximately 1,600 nmi. The characteristics of the DMSP primary sensors are described in greater detail in the Navy Tactical Applications Guide, Volume I (Fett and Mitchell 1977).

The spectral interval of the visible channel is 0.4-1.1 μm. The sensor normalized response curve is shown in Figure 2-1. The curve indicates that the peak response is at 0.8 μm with the sensor's half-power response points at 0.57 μm and 0.97 μm. Most of the energy received, therefore, is at the longer visible wavelength and the near-infrared wavelengths where vegetation is highly reflective; as a result, very good contrast is achieved between vegetation, soil, and water surfaces. The lesser response at the short wavelengths also minimizes the blue-light backscattering of the atmosphere.

2.1.2 Data Display and Enhancement

The VHR data are displayed either in a scale of 1:15 million (normal mode) or 1:7.5 million (expanded mode). The images analyzed in the study were the fine resolution (0.3 nmi) data at the 1:15 million scale and were in the form of transparencies. Examples of DMSP images are shown in Section 4.

Contrast enhancement is used at the DMSP receiving stations to vary the distribution of gray shades in the data. This capability is of particular importance in the detection of anomalous gray-shade patterns, since these patterns are at the darker end of the overall tonal scale of the image. The mapping curves devised for the various enhancements are shown in Figure 2-2.

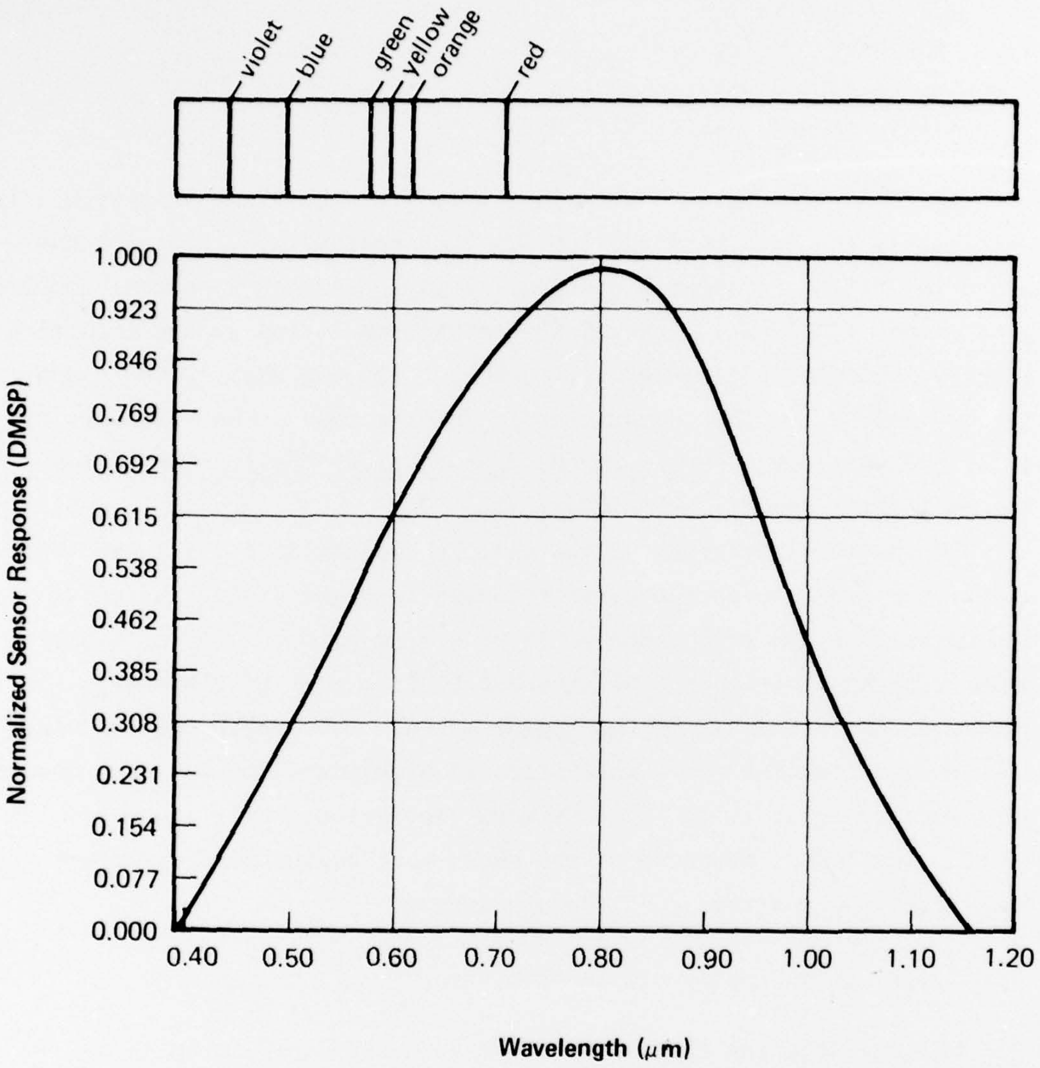

Figure 2-1 DMSP Normalized Sensor Response

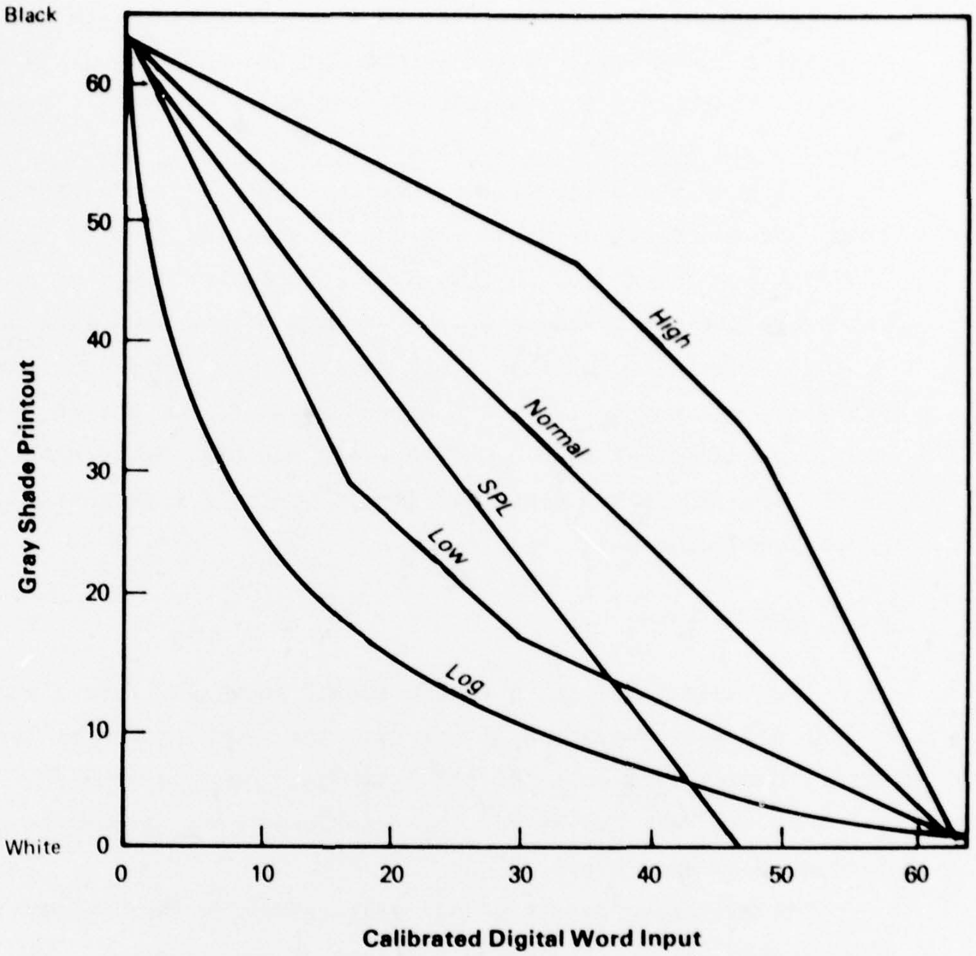

Source: Fett and Mitchell 1977

811265a

Figure 2-2 Various Enhancement Curves for DMSP Images

The normal enhancement mode is a linear scale, with gray-shade definition evenly distributed throughout the total tonal range from white to black. In the log enhancement mode, however, the calibrated digital word input at the lower end of the scale is output over a wider range of gray-shade levels; as seen in Figure 2-2, the digital input from 0 to 13 is output as a gray-shade variation from 63 (black) to 20 (light). Therefore, in this mode, the darker range of gray-shade values is greatly enhanced at the expense of the much lighter tones, so that anomalous gray shades are more clearly depicted. Darker tones are also enhanced in the low-enhancement mode, but not as well as in the log enhancement mode. In contrast, the high enhancement mode suppresses the darker tones, so is not useful for depicting anomalous gray-shade patterns.

2.2 Landsat Data

The Landsat MSS has a resolution of about 240 feet (80 m), compared to the 0.3 nmi resolution of the VHR. The swath viewed by the radiometer, however, is only 100 nmi (185 km) wide, compared to the 1,600 nmi swath of the VHR. Moreover, the same area on the ground is covered by Landsat only once every 18 days.

The MSS measures reflected solar energy in four spectral bands in the visible and near-infrared portions of the spectrum. The four bands are: (1) MSS-4 (0.5-0.6 μm, blue-green); (2) MSS-5 (0.6-0.7 μm, red); (3) MSS-6 (0.7-0.8 μm, red to near infrared); and (4) MSS-7 (0.8-1.1 μm, near infrared).

The normalized spectral response curves of the four bands are shown in Figure 2-3; for comparison, the DMSP response is also shown in the same figure. This figure illustrates that approximately 45% of the DMSP response is at the Landsat MSS-7 wavelength. About 25% of the response is at the MSS-6 wavelength, 20% at MSS-5, and only 10% at MSS-4.

The MSS data are displayed in scenes covering 100 nmi square. The standard scale of a scene is 1:1 million. Most of the scenes used in the analysis were acquired in the transparency format. Examples of the Landsat data are included in Section 4.

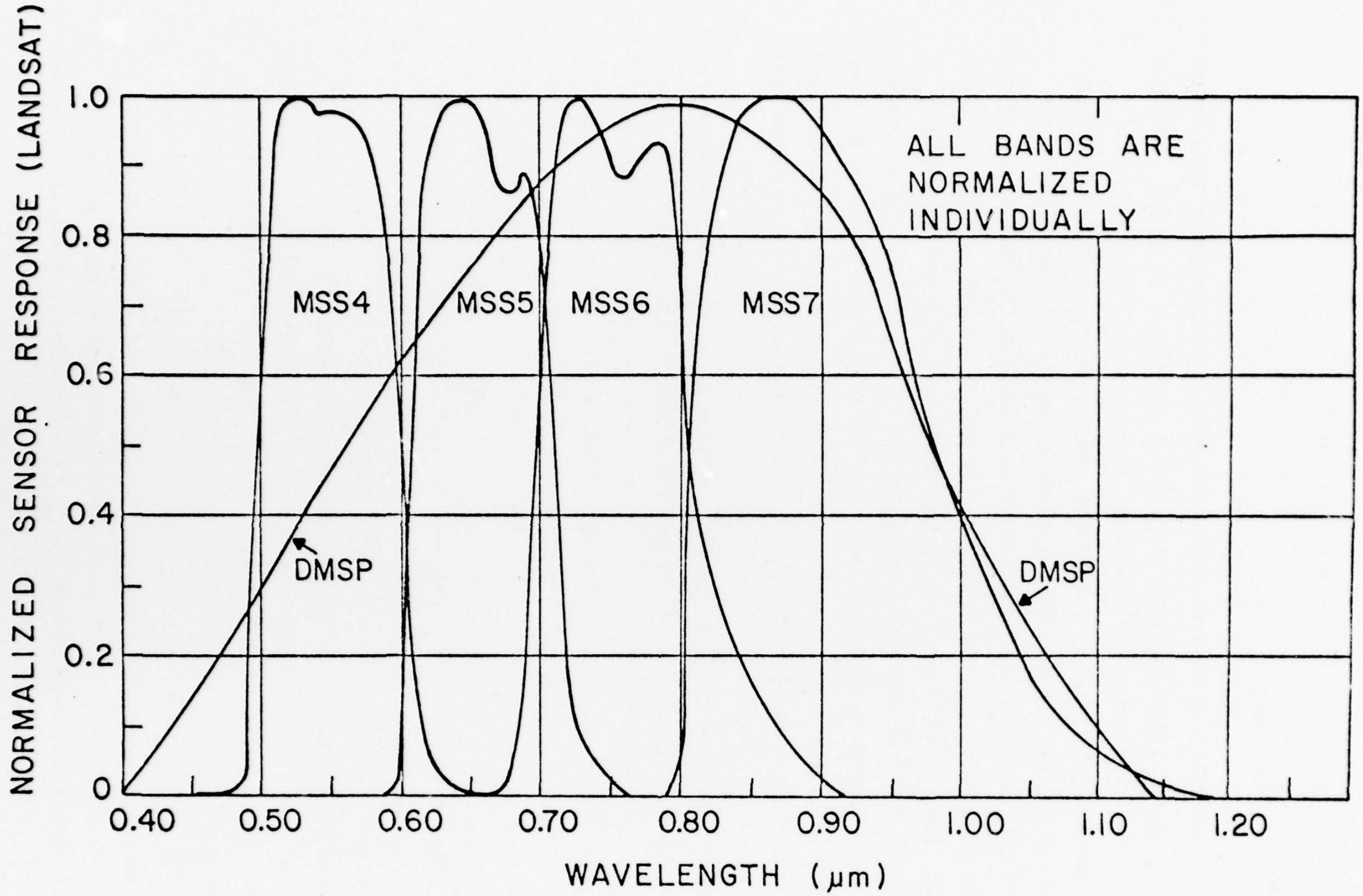

Figure 2-3 Landsat Relative Spectral Response (DMSP Spectral Response is Also Shown)

Source: Norwood et al 1972

2.3 Detection of Anomalous Gray-Shade Patterns

2.3.1 DMSP Data

Several examples of anomalous gray-shade patterns are presented in the Navy Tactical Applications Guide (Fett and Mitchell 1977). Basically, the term is applied to the light tone and occasional dark tone gray-shade patterns observed over ocean or land areas in cloud-free or nearly cloud-free regions in the VHR (visible) imagery. (It should be noted that "light tone" nevertheless refers to a tone at the darker end of the overall tonal range of the image, as opposed to "bright tones" of clouds or heavy fog.) The interpretation given to the anomalous gray-shade patterns is important because it can provide insight into the atmospheric and/or oceanographic processes occurring in the area; additionally, the reduced visibilities that may be associated with the patterns detectable in the satellite imagery could have impact on a variety of naval weapons systems.

Fett and Mitchell (1977) point out that anomalous gray-shade patterns can be caused by a number of factors, including: the presence or absence of atmospheric moisture in cloud-free areas, the presence of broken fields of small cumuliform cells below the sensor resolution, cirrus clouds, dust or sandstorms, ocean spray, turbid water or bottom features in shallow water areas, and haze and light fog in areas of developing or dissipating fog or stratus. For the purposes of this study, the patterns of interest were those caused by light fog and/or haze conditions associated with reduced visibilities. No analyses were performed of patterns known to be caused by other factors.

A DMSP VHR image showing an anomalous gray-shade pattern off the California coast is presented by Fett and Mitchell (1977) as an example of a pattern associated with a light fog situation. In the discussion of that case, the authors conclude that: (1) anomalous gray-shade bands are often the high humidity end products of stratus/fog band dissipation; (2) light-tone gray-shade areas, remote from sunglint patterns, at the edges of stratus/fog or stratocumulus are regions of high humidity associated with a concentration of large-size condensation particles and haze (low-level visibilities are generally reduced in these areas); and (3) dark-tone gray-shade areas adjacent to lighter-tone gray-shade areas, remote from sunglint, are regions of lower humidity and less hazy conditions (low-level visibilities are generally higher in these areas).

2.3.2 Landsat Data

Landsat is designed to view the earth's surface, rather than the atmosphere, and has been used primarily for that purpose. Nevertheless, Landsat data have been found quite useful for studies of mesoscale cloud features (Feteris et al. 1976). In addition, studies of the use of Landsat to detect atmospheric aerosols have been carried out by several investigators, including Fraser (1976) and Griggs (1978). Landsat imagery was also examined in a study of air pollution patterns in New England using remote sensing data (Bowley et al. 1977).

In his study reported in 1976, Fraser determined the mass of particulates in a vertical column of dust outflow from northwestern Africa with the aid of Landsat measurements of nadir radiance. The mass of dust was also estimated from the nadir radiance of a radiative transfer model of the ocean-atmosphere system. The computed radiance agreed within 10% of the radiance measured by satellite. Fraser also compared the radiance measured by each of the four Landsat MSS bands for various locations over the ocean and a high-altitude lake. As to be expected because Rayleigh scattering is large at the shorter wavelengths, the radiance measured by the MSS-4 band (0.5-0.6 μm) was found to be the greatest in each case; decreasing radiances were measured by the MSS-5 through 7 bands, respectively, except for one case where the MSS-6 value was less than the MSS-7 value.

Griggs (1978) determined the aerosol content in the atmosphere from Landsat using a large set of data and found good agreement between the measured radiances over the ocean and the aerosol content, especially for the MSS-5 and MSS-6 bands. In his study, Griggs discussed some of the potential problems affecting the Landsat measurements. Over inland water areas, the first three bands (MSS-4, 5, and 6) can be affected by water pollution; the MSS-7 band is affected less by water pollution, so is the best band for measuring aerosols over these areas. Over the ocean, the potential problems include sunglint, wind shadow, and observations of internal waves. However, Griggs points out that internal waves are observed only in areas with both calm seas and sunglint, and should, therefore, not affect the measurements in nonsunglint areas.

3. COLLECTION OF DATA SAMPLE

3.1 Data Sources

3.1.1 DMSP

Initial attempts to obtain selected DMSP images were conducted through the University of Wisconsin, Space Science and Engineering Center, where a complete archive of data is maintained. The acquisition of imagery from this source proved unsuccessful in most instances because DMSP coverage for some of the selected areas was not available. Moreover, all of the DMSP imagery available from this data source were the normal enhancement mode rather than either the low- or log-enhancement modes, which are needed to depict the anomalous gray-shade patterns (see Section 2.1.2). Useful data were eventually obtained on loan from Keesler Air Force Base and from the Naval Environmental Prediction Research Facility.

3.1.2 Landsat

The determination of whether correlative Landsat coverage existed for selected dates and areas of potentially good haze or light-fog situations was accomplished through use of the query-search capability available at the EROS Data Center, Sioux Falls, South Dakota. Once particular Landsat scenes were selected for analysis, the images (four spectral bands) were acquired from the National Oceanic and Atmospheric Administration (NOAA) Satellite Data Services Division (SDSD).

3.2 Data Search Procedures

Several methods were used to obtain useful cases of correlative DMSP/Landsat coverage viewing anomalous gray-shade patterns. Because of the infrequent Landsat coverage as compared to the DMSP coverage, the data search initially concentrated on determining the availability of Landsat coverage for selected coastal areas during the period from April through September 1977. (The DMSP Block 5C data first became available in April 1977.) Five areas were selected: (1) the Northeast (40°-46°N, 68°-74°W); (2) the mid-Atlantic coast (36°-40°N, 72°-76°W); (3) California (32°-38°N, 117°-124°W); (4) the Washington/Oregon coast (43°-48°N, 122°-126°W); and (5) the Gulf of Alaska (50°-55°N, 140°-150°W).

Surface charts for April-September 1977 were reviewed for each of the five areas, and dates with reported low visibility conditions caused by haze and light fog were documented. These dates were then checked against the query-search computer listing obtained for each area to determine dates with correlative Landsat coverage. A number of potential cases were determined for all of the areas except the Gulf of Alaska region, for which Landsat coverage was unavailable during the April-September 1977 period.

A review of DMSP imagery for the two East Coast areas, received on loan from Keesler AFB, was conducted to determine whether any anomalous gray-shade patterns were detectable. In many instances, either no such patterns were observed within the areas of reported low visibility, or considerable amounts of cloud cover were present. Also, for a number of dates, no log- or low-enhancement DMSP images were available. Based on this examination, a total of seven East Coast cases were selected for preliminary analysis.

A search for additional cases was conducted through examination of DMSP images received from the University of Wisconsin archives for the two West Coast areas. The extents of gray-shade areas were noted and checked carefully against the coordinates of correlative Landsat scenes, as determined from the query-search listing. The results of these comparisons were disappointing as concurrent Landsat coverage, in all but one case, fell outside the area of anomalous gray shade in the corresponding DMSP image.

In addition to these data searches, a check with the EROS Data Center also indicated that concurrent Landsat coverage did exist for two anomalous gray-shade areas discussed by Fett and Mitchell (1977). The DMSP images for these two cases were obtained from the Naval Environmental Prediction Research Facility.

Review of the initially selected cases indicated that some of these cases were questionable owing to the relatively poor quality of the DMSP imagery received from the two data sources, as compared to the enhanced images shown by Fett and Mitchell (1977). Very few of the images acquired from the archives at either the University of Wisconsin or at Keesler AFB were of comparable quality. Subsequently, approximately 30 additional DMSP images where anomalous gray-shade patterns were observed within areas of reported low-visibility conditions were acquired from the Naval Environmental Prediction Research Facility. A check of Landsat coverage indicated that correlative Landsat imagery was available for seven of these cases.

3.3 Discussion of Problems in Case Selection

As expected, the major problem was obtaining correlative Landsat coverage within the exact area of the anomalous gray-shade pattern. In a number of instances when concurrent Landsat imagery was available, the location of the particular scene or scenes fell just outside the region of interest. In addition, on a number of occasions, the Landsat MSS-4 or MSS-5 band, or both, were unavailable in the data file.

Another problem that frequently arose was the lack of either the log- or low-enhancement DMSP data from the archives of either data source; furthermore, even when the low-enhancement products were available, the overall quality of some of the images was not acceptable for detection of subtle gray-shade patterns. The verification of light fog or haze situations over coastal waters or open ocean areas was also impossible at times owing to the lack of ship weather observations within the gray-shade areas as depicted in the DMSP images.

It should be noted that because of the expense in acquiring Landsat data, the corresponding Landsat images were acquired only for cases where anomalous gray-shade patterns had been detected in the DMSP image. It was not possible, therefore, to determine whether any cases existed where a haze pattern was evident in the Landsat data, but was not detectable in the corresponding DMSP image. As has been pointed out above, however, anomalous gray-shade patterns were not always detectable in DMSP images covering areas with reported low visibilities.

3.4 Cases Acceptable for Analysis

The following is a listing of cases that were determined to be acceptable based on the presence of anomalous gray-shade patterns in the DMSP imagery, available correlative DMSP and Landsat imagery, and available weather observations that supported the presence of a reduced visibility situation in light fog or haze.

20 July 1973; over water; Gulf of Tonkin, Viet Nam
22 May 1974; over water; California Coast, United States
29 July 1975; over land; Southeastern United States
30 July 1975; over land; Midwestern United States
7 August 1975; over land; Northern Italy
15 August 1975; over land; Mid-Atlantic Coast, United States
4 September 1975; over land; Mid-Atlantic Coast, United States
5 September 1975; over land; Mid-Atlantic Coast, United States
14 October 1975; over land; Southeastern United States
27 April 1977; over water; New England Coast, United States
22 June 1977; over water; California Coast, United States
14 July 1977; over water; Mid-Atlantic Coast, United States
18 July 1977; over water; Mid-Atlantic Coast, United States
19 July 1977; over water; Mid-Atlantic Coast, United States
17 August 1977; over water; East Coast, United States
19 August 1977; over water; Mid-Atlantic Coast, United States
23 August 1977; over water; Mid-Atlantic Coast, United States
3 September 1977; over water; Northeastern United States
4 September 1977; over water; New England Coast, United States
20 September 1977; over water; East Coast, United States

3.5 Final Case Selection

A number of the initial cases became unacceptable for one or more of the reasons discussed previously, such as lack of precise Landsat coverage within the area of gray-shade pattern, poor quality DMSP resulting in marginal anomalous gray shades, sunglint on DMSP imagery, missing bands on the Landsat imagery, or poor timing between Landsat and DMSP. The cases selected for detailed analysis are listed below; the analysis of these cases is discussed in Section 4.

Case 1: 22 May 1974; over water; California Coast, United States
Case 2: 29 July 1975; over land; Southeastern United States
Case 3: 15 August 1975; over land; Mid-Atlantic Coast, United States
Case 4: 4 September 1975; over land; Mid-Atlantic Coast, United States
Case 5: 5 September 1975; over land; Mid-Atlantic Coast, United States
Case 6: 30 July 1975; over land; Midwestern United States
Case 7: 7 August 1975; over land; Northern Italy
Case 8: 14 October 1975; over land; Southeastern United States.

4. COMPARATIVE ANALYSIS OF DMSP AND LANDSAT IMAGERY FOR SELECTED CASES

The comparative analysis of DMSP and Landsat multispectral imagery for the eight cases listed in Section 3.5 is presented below. The DMSP images for the first two cases are also discussed by Fett and Mitchell (1977).

4.1 Case 1: 22 May 1974 - Southern California Coast (over water)

A low-enhancement DMSP VHR image taken at 1613 GMT (0913 PDT) on 22 May 1974 shows an early morning fog/stratus band off Point Arguello, California (Figure 4-1). Another low-enhancement VHR image taken over two hours later (1850 GMT) shows that the intial fog/stratus band had dissipated, now appearing as an area of anomalous gray shade (Figure 4-2).

A Landsat pass occurred at 1806 GMT, 44 minutes prior to the time of the second DMSP image, which shows the anomalous gray shade (the area covered by the Landsat image is indicated in Figure 4-2). The Landsat MSS-4 and MSS-5 band images are shown in Figures 4-3a and 4-3b, the MSS-6 and MSS-7 band images are shown in Figures 4-4a and 4-4b.

Although no surface weather observations fell within the boundaries of the Landsat image, it is apparent that the gray-shade pattern observed in the DMSP image was probably caused by a combination of high humidity and small stratocumulus cloud cells. Most likely, the early morning fog/ stratus located off Point Arguello had dissipated somewhat and risen to form a layer of stratocumulus clouds. In the MSS-4 band, there is some haze associated with the clouds. The haze can also be detected in the MSS-5 band, but not at all in the MSS-6 band. In the MSS-7 band, only the cloud immediately over the coastal region is observed. Two distinct brighter cloud (or fog) areas are seen in the Landsat images along the coast (Figure 4-3); in the second DMSP image, however, the whole area is an anomalous gray shade with no difference in tone at those particular places (Figure 4-2). It is possible that during the 44-minute time period between the Landsat observation and the second DMSP observation, dissipation in the cloud/fog areas occurred to the point where these areas are no longer evident in the DMSP image. In the

Figure 4-1 Low Enhancement DMSP VHR Image at 1613 GMT on 22 May 1974 with Area of Correlative Landsat Imagery Outlined

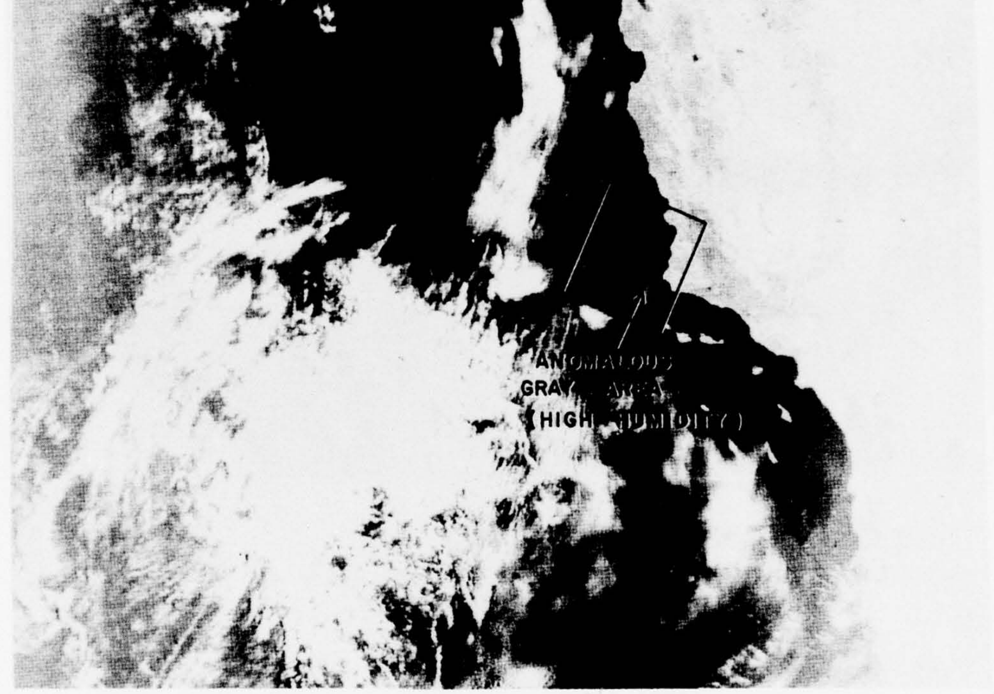

Figure 4-2 Low Enhancement DMSP VHR Image at 1850 GMT on 22 May 1974 with Area of Correlative Landsat Imagery Outlined

Figure 4-3a Landsat MSS-4 Image (1668-18062) at 1806 GMT on 22 May 1974 with Corresponding Anomalous Gray Shade Area Outlined

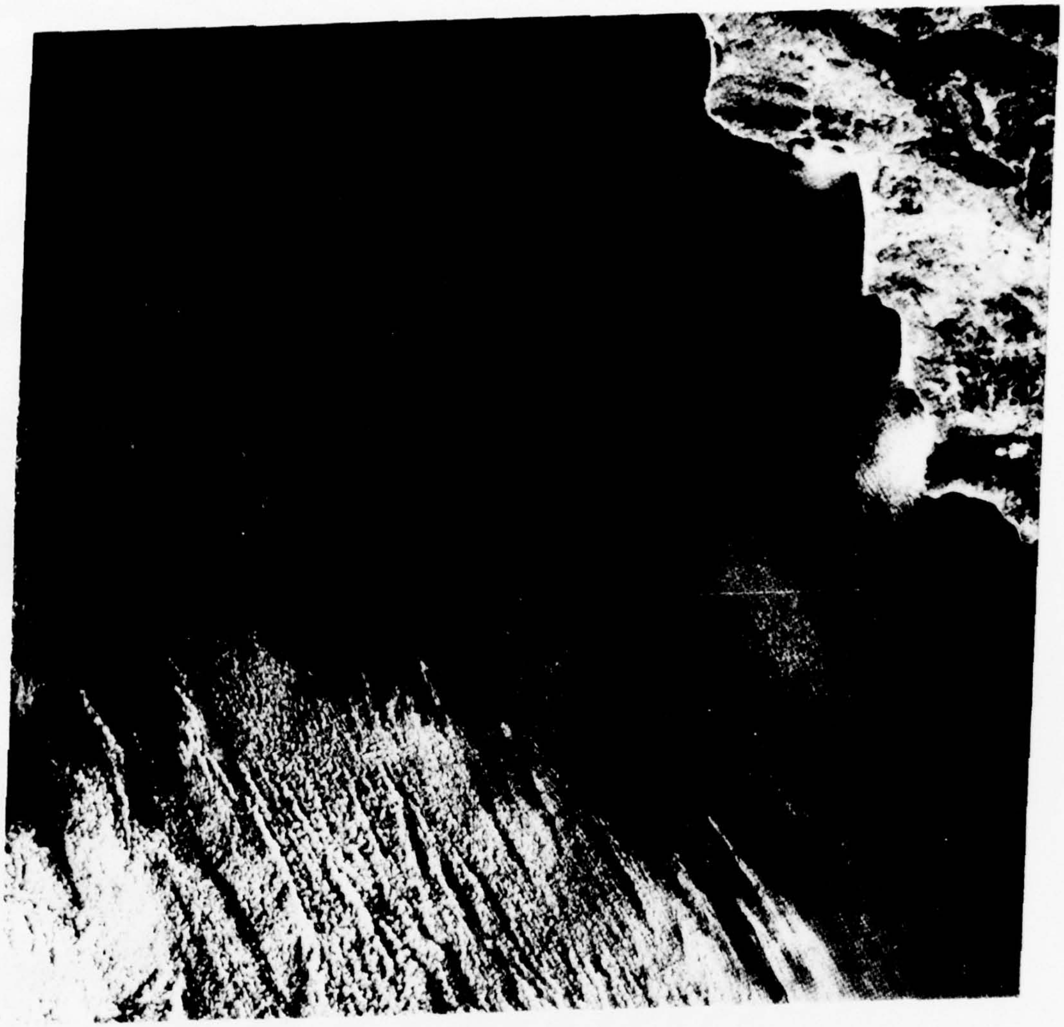

Figure 4-3b   Landsat MSS-5 Image (1668-18062) at 1806 GMT on 22 May 1974

Figure 4-4a Landsat MSS-6 Image (1668-18062) at 1806 GMT on 22 May 1974

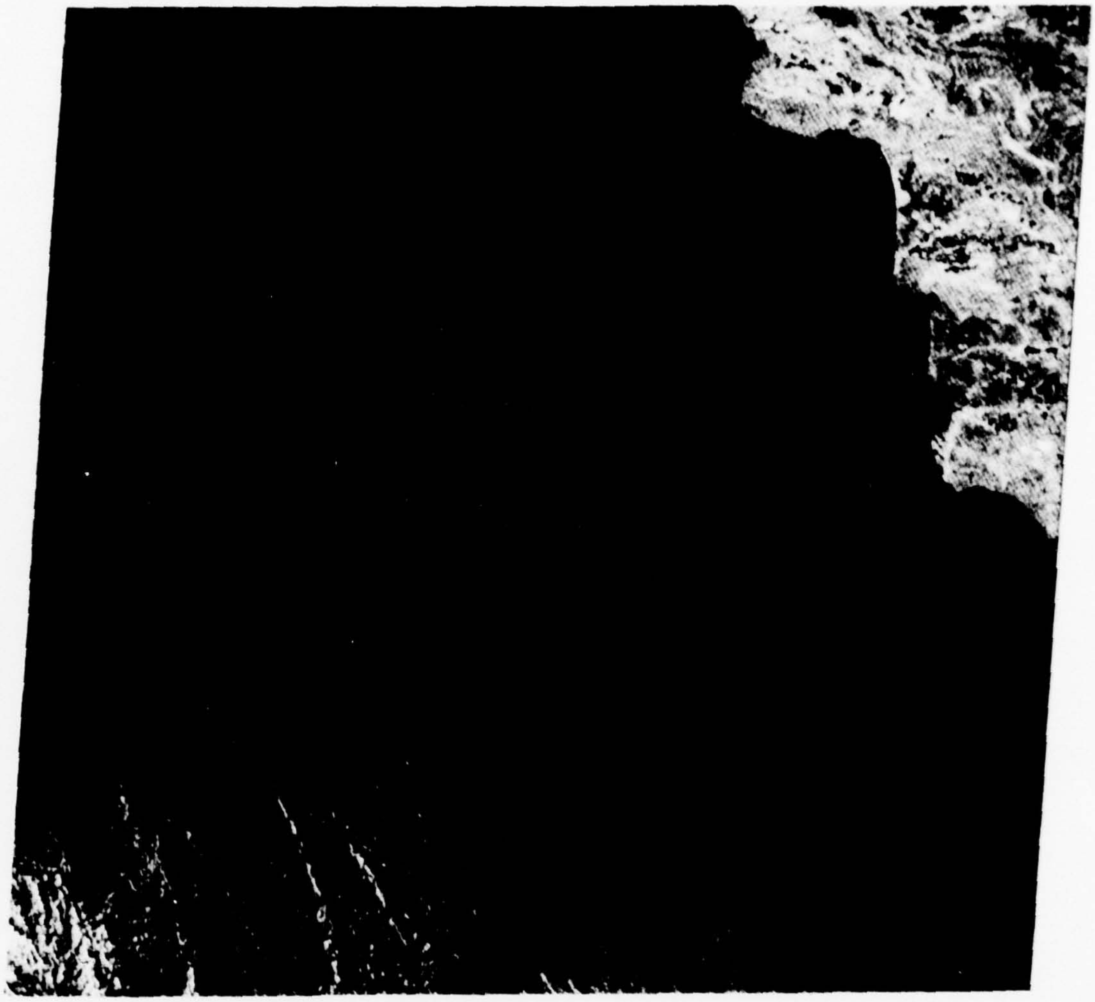

Figure 4-4b Landsat MSS-7 Image (1668-18062) at 1806 GMT on 22 May 1974

Landsat image, especially MSS-5, small "dark" areas are seen along the coast (Figure 4-3b); these patterns were probably caused by calmer waters in the lee of the land, as compared to rougher waters just offshore under the influence of strong winds.

The 1800 GMT surface weather reports showed that the moisture associated with the initial fog situation was confined to the coastal regions as the lower atmosphere is very dry just inland from the coast. There was a frontal system approaching from the northwest, associated with a deep trough in the Gulf of Alaska, and another weak trough located southwest of the anomalous gray area; however, there was no significant weather associated with it at that time. The winds offshore were strong (averaging 15-20 knots) from the north-northwest and, in general, the ocean waters were rough except in sheltered coastal regions.

4.2 Case 2: 29 July 1975 - Southeastern United States (over land)

A low-enhancement DMSP VHR image of 29 July 1975 (1433 GMT), shown in Figure 4-5, displays a band of high reflectance associated with reported ground fog and clouds. Just south of the bright band is an anomalous gray-shade pattern, with distinct tonal steps, located over Kentucky, Tennessee, and the Carolinas. This gray-shade pattern appears to be associated with haze, smoke, and high humidity within moist tropical air advecting northward ahead of a tropical depression that had just moved inland from the Gulf of Mexico. The elongated bright band and anomalous gray shades are located in the peripheral subsidence area ahead of the storm system. Surface temperatures within the anomalous gray-shade region were reported to be 19°-24°C (66°-75°F) at the time of the DMSP observation with a temperature dew-point spread of only 1°-2°C. Also, visibilities were reported to be generally under three miles in haze, ground fog, and/or smoke.

A correlative Landsat scene for the area indicated in Figure 4-5 was taken at 1530 GMT (about an hour after the DMSP observation). The four MSS bands are shown in Figures 4-6a to 4-6d. In the Landsat images, the bright cloud/fog area is easily recognizable. In addition, a hazy, gray tone can be seen in the MSS-4 and MSS-5 bands (Figures 4-6a and 4-6b) within the region of anomalous gray-shade pattern displayed on the

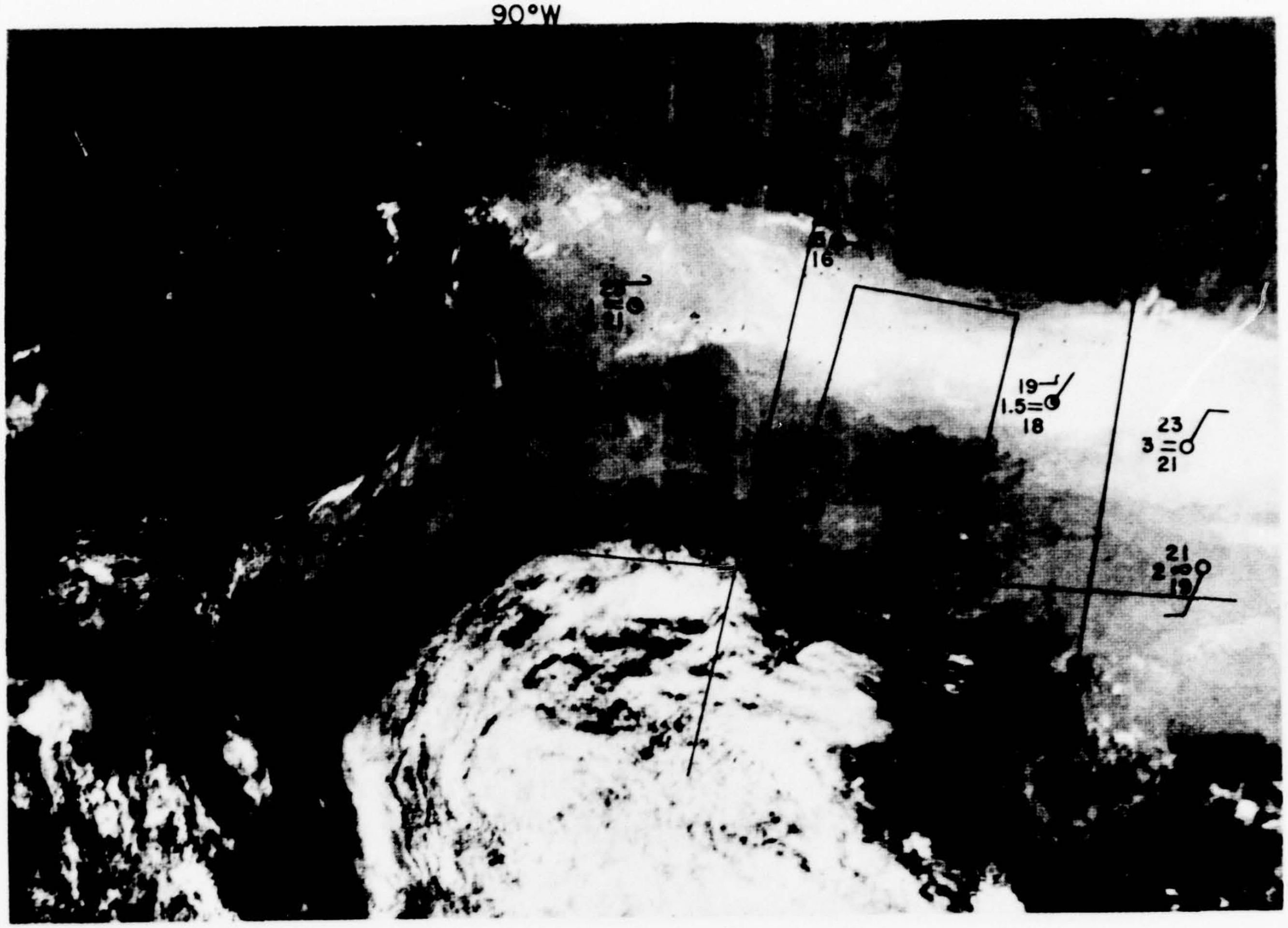

Figure 4-5 Low Enhancement DMSP VHR Image at 1423 GMT on 29 July 1975 with Area of Correlative Landsat Imagery Outlined and 1200 GMT Surface Weather Observations Shown

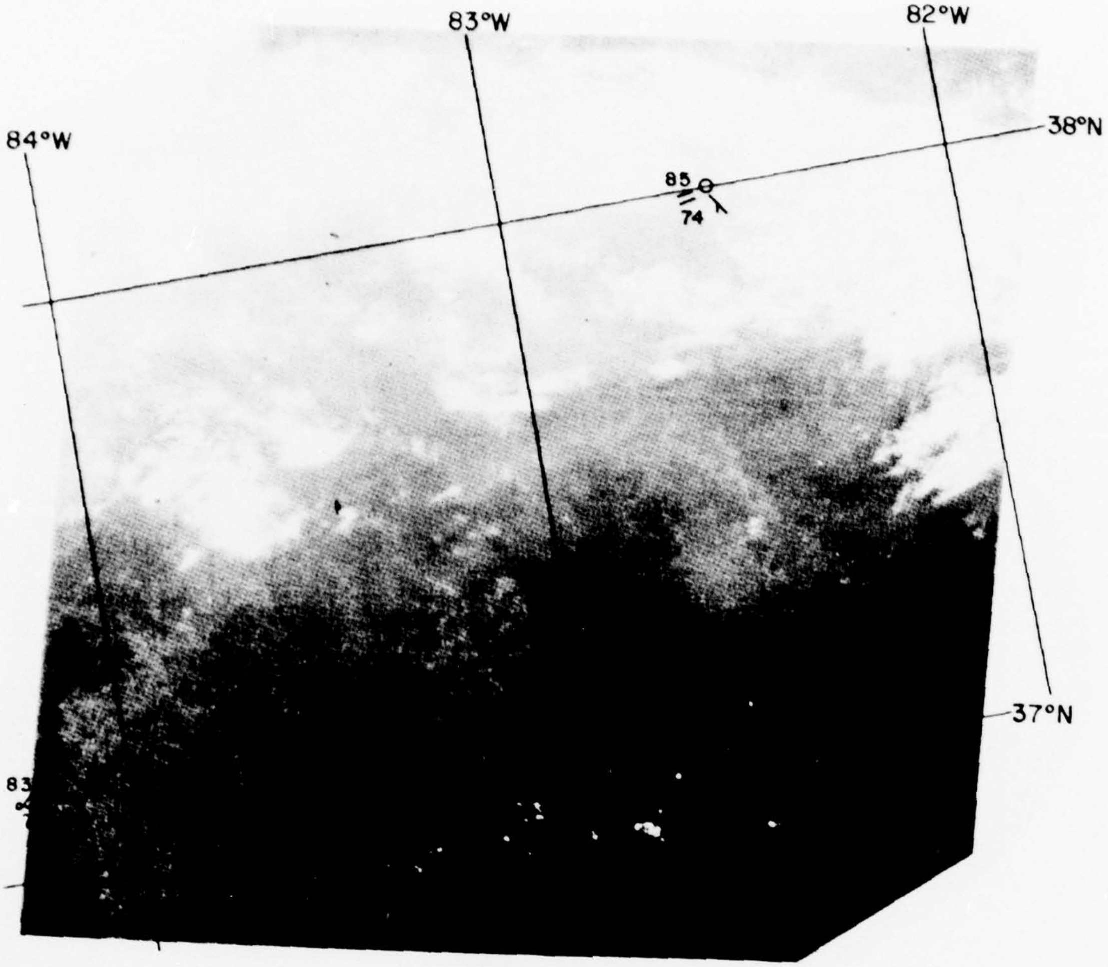

Figure 4-6a Landsat MSS-4 Image (2188-15305) at 1530 GMT on 29 July 1975 with 1200 GMT Surface Weather Observations Shown

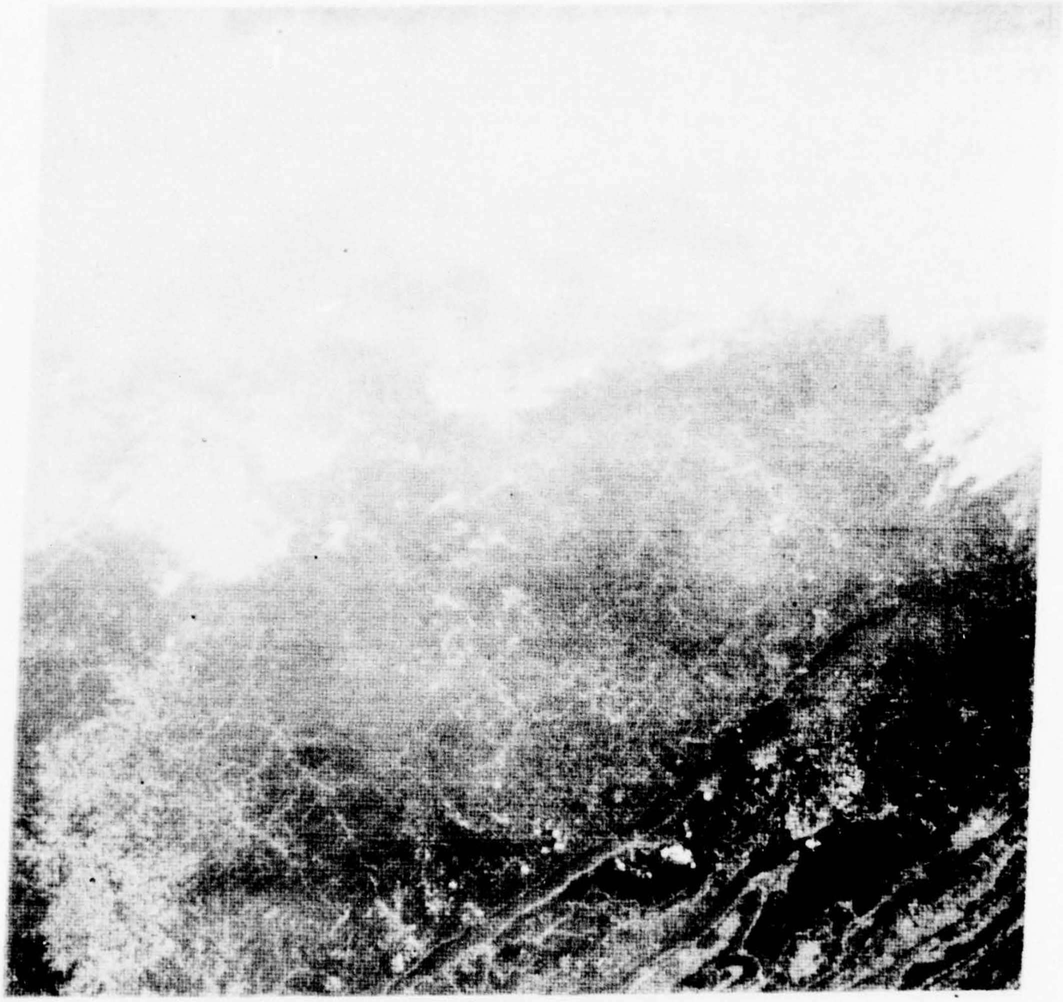

Figure 4-6b Landsat MSS-5 Image (2188-15305) at 1530 GMT on 29 July 1975

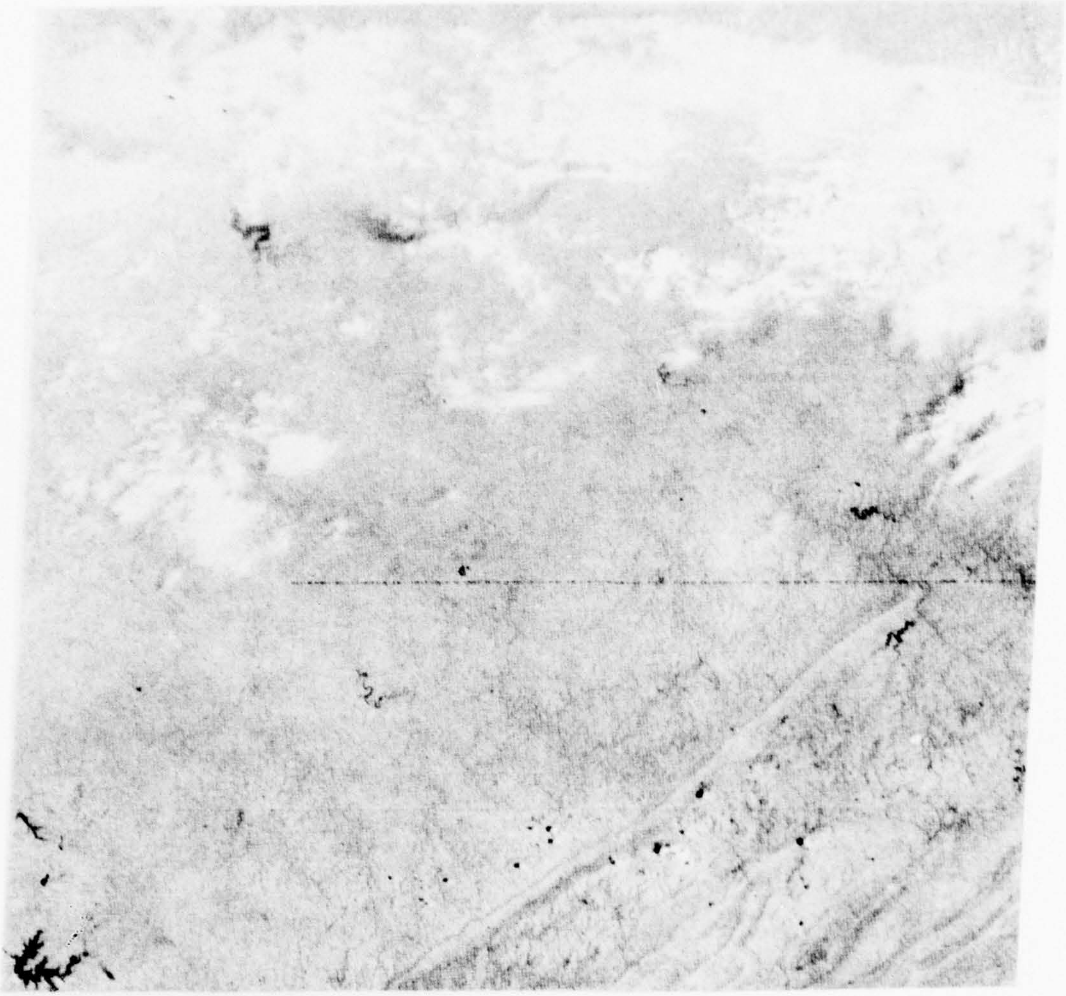

Figure 4-6c Landsat MSS-6 Image (2188-15305) at 1530 GMT on 29 July 1975

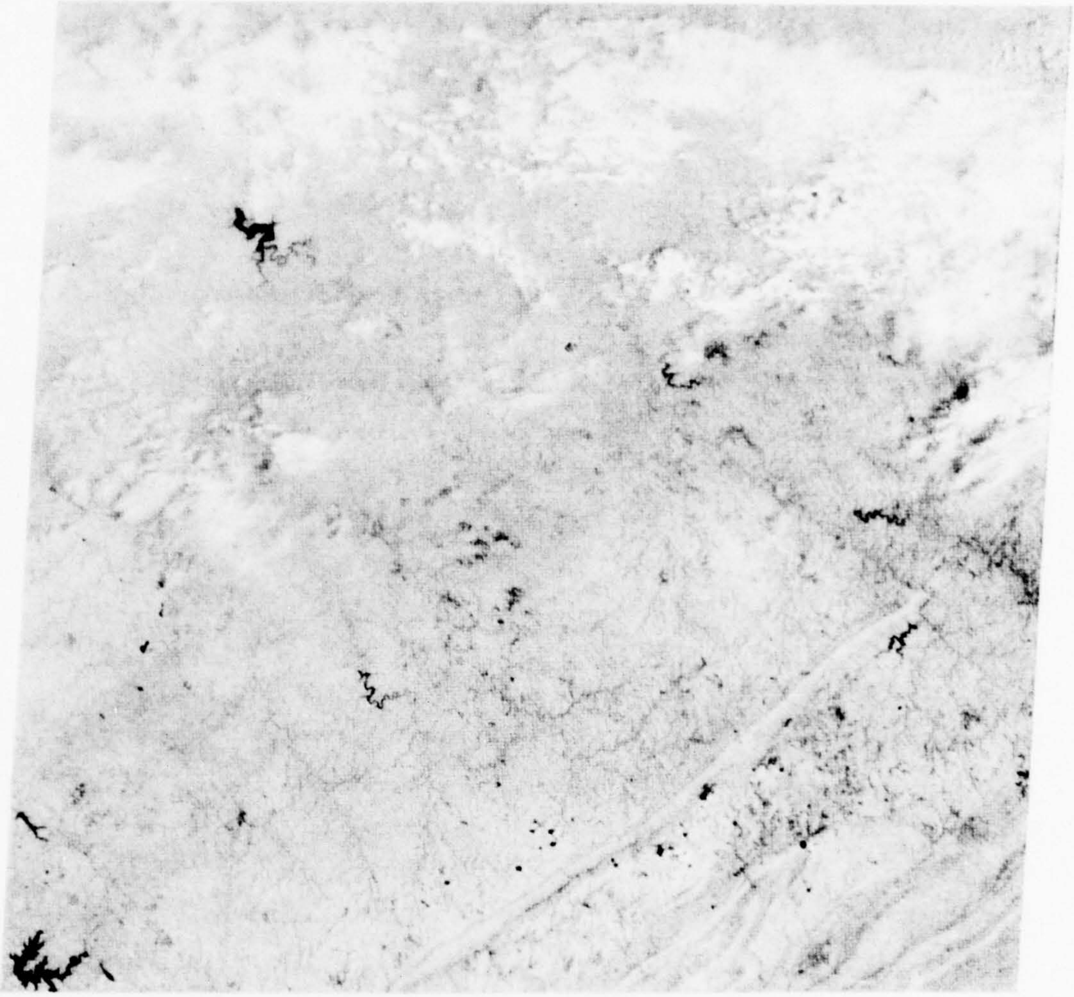

Figure 4-6d Landsat MSS-7 Image (2188-15305) at 1530 GMT on 29 July 1975

DMSP image. Further comparison of the DMSP and Landsat MSS-4 and MSS-5 bands shows, however, that the distinct boundaries of gray-shade tones displayed on the DMSP image are not detectable in the Landsat images. Two surface reports (Figure 4-6b) indicated that temperatures had risen to 30°C (86°F) by 1500 GMT.

The MSS-6 and MSS-7 bands of the Landsat scene, shown in Figures 4-6c and 4-6d, display a considerably brighter terrain background, as compared to the MSS-4 and MSS-5 bands. The MSS-6 band (Figure 4-6c) displays a slight indication of haziness when compared to the MSS-7 band (Figure 4-6d); the contrast in MSS-7 is much sharper, especially over the lake in the upper left corner of the image, and there is also considerably less "fuzziness" over the terrain. The MSS-6 and 7 data also clearly reveal the presence of considerable cumuliform cloudiness within the region of the bright band displayed on the DMSP image. The water bodies within the scene, especially the lake in the northwest corner, can be used as a reference in comparing the various spectral bands; this lake cannot be detected in the MSS-4 and 5 bands but is readily detected in the near-infrared bands.

As seen in Figure 4-6a to 4-6d, large patterns may be difficult to detect in Landsat images over land areas because of the highly variable reflectance of the terrain background. Moreover, the high reflectance of vegetation in the near infrared (MSS-6 and especially MSS-7) makes it extremely difficult to detect subtle cloud/haze patterns in those bands. As noted above, however, the cloud area in the MSS-7 band is seen to consist of both cumuliform and cirriform clouds; considerable detail in the clouds is lost in the visible bands.

4.3 Case 3: 15 August 1975 - Mid-Atlantic Coast (over land)

An excellent example of multilayered anomalous gray shades is readily seen on the low-enhancement DMSP VHR imagery taken at 1422 GMT (Figure 4-7). The area of anomalous gray shade is confined to portions of Virginia, North Carolina, and Tennessee. The areas covered by two correlative Landsat scenes and the 1200 GMT surface weather observations are indicated in Figure 4-8. The hatched area indicated inside the boundaries of the Landsat scenes defines the anomalous gray shade appearing on these images.

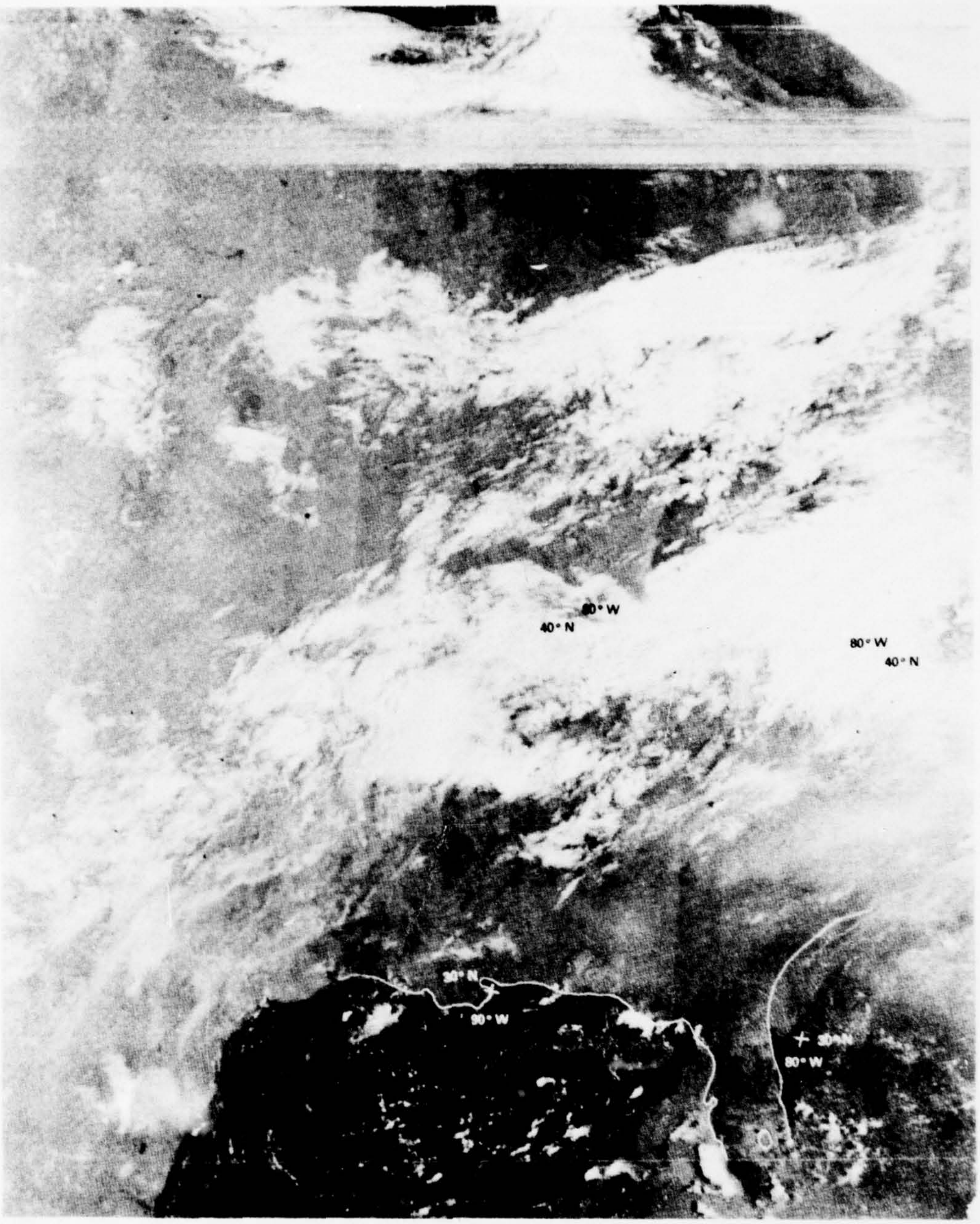

Figure 4-7 Low Enhancement DMSP VHR Image at 1422 GMT on 15 August 1975

Figure 4-8 Low Enhancement DMSP VHR Image at 1422 GMT on 15 August 1975 with Area of Correlative Landsat Imagery Outlined and 1200 GMT Surface Weather Observations Shown

The Landsat observation, which was taken only one hour after the DMSP image, covers a good portion of the anomalous gray area. The MSS-4 image (Figure 4-9) is extremely hazy over the entire area viewed. The MSS-5 image is slightly hazy, whereas the MSS-6 and 7 images are relatively clear (MSS-7 is shown in Figure 4-10). It is interesting to note that in the MSS-4 image the upper left-hand corner has the same cloud band (mostly cumulus) that can be seen on the DMSP image, and the lower right-hand corner is somewhat clearer, reflecting that portion of the image outside the area of anomalous gray as is depicted on the DMSP overlay (Figure 4-8). The MSS-4 image for the adjacent scene, shown in Figure 4-11, views an area just north of the boundary of the brightest anomalous gray area in the DMSP; consequently MSS-4 is only slightly hazy, and the MSS-5, 6, and 7 bands are clear. The same cloud patterns that are seen on the DMSP image can be identified in the upper-left corner of Figure 4-11.

North and west of the anomalous gray region there were numerous light showers and thunderstorms extending along a stationary front from Maryland to a weak low center over Chicago and extending southeastward through Oklahoma into the Texas Panhandle. This was the furthest southern penetration of any front over the past week as the upper-air flow had remained weak and predominantly from the south. In the southeast corridor, in the region where the anomalous gray shade is located, there was a broad area of fog and haze with visibilities generally less than four miles and dew point temperatures of 21-24°C (70s°F) (Figure 4-8).

4.4 Case 4: 4 September 1975 - Mid-Atlantic Coast (over land)

A low-enhancement DMSP VHR image of 1458 GMT on 4 September 1975, shown in Figure 4-12, displays a well-defined anomalous gray-shade pattern located over parts of Kentucky, Tennessee, Mississippi, and Arkansas. The location of two correlative Landsat scenes, taken 38 minutes later at 1536 GMT, and the 1500 GMT surface weather observations for stations in the area are shown in Figure 4-13.

The MSS-4 band images for the two Landsat scenes (Figures 4-14 and 4-15) view the region of anomalous gray-shade pattern showing the maximum brightness on the DMSP image. These visible band images each

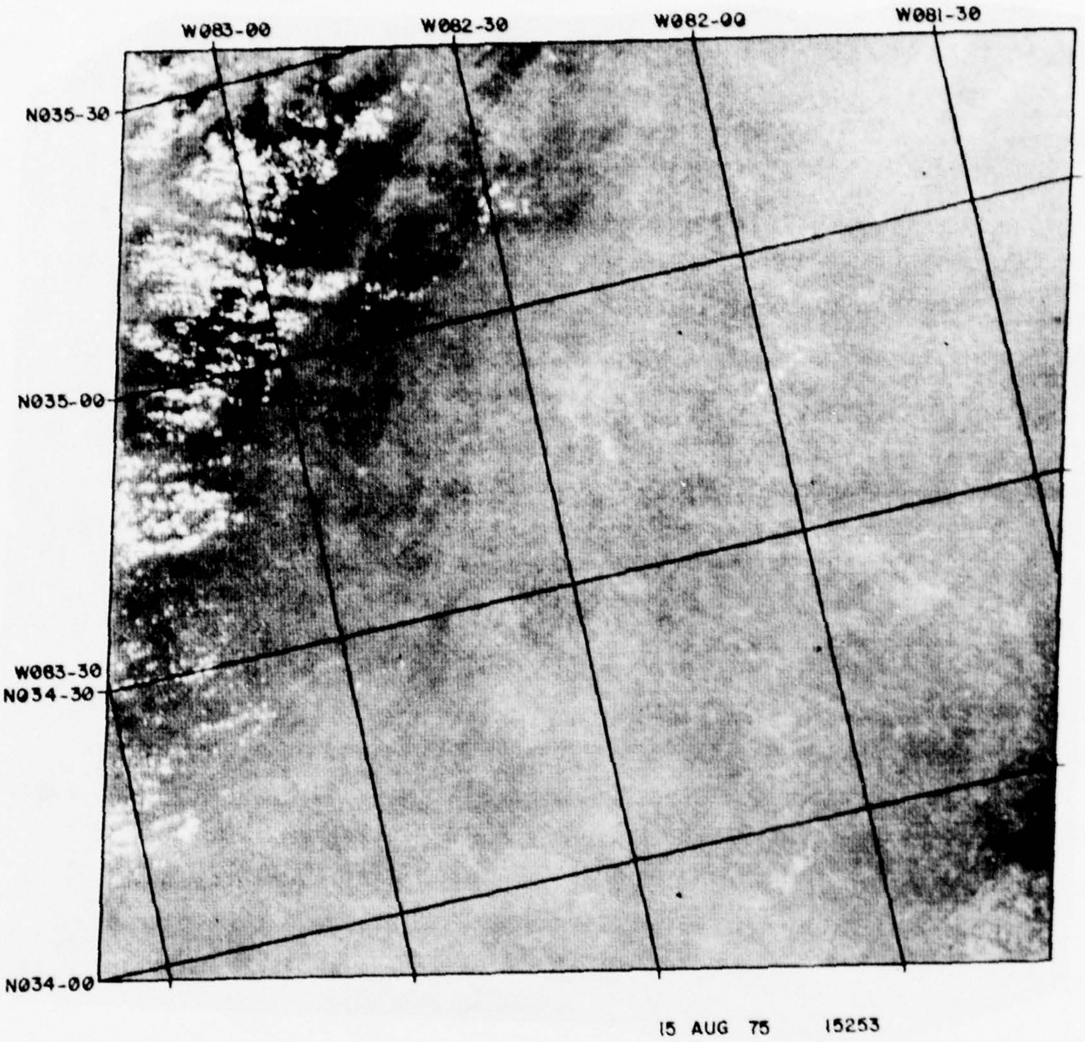

Figure 4-9 Landsat MSS-4 Image (2205-15253) at 1525 GMT on 15 August 1975. (This scene corresponds to the lower area outlined in Figure 4-8)

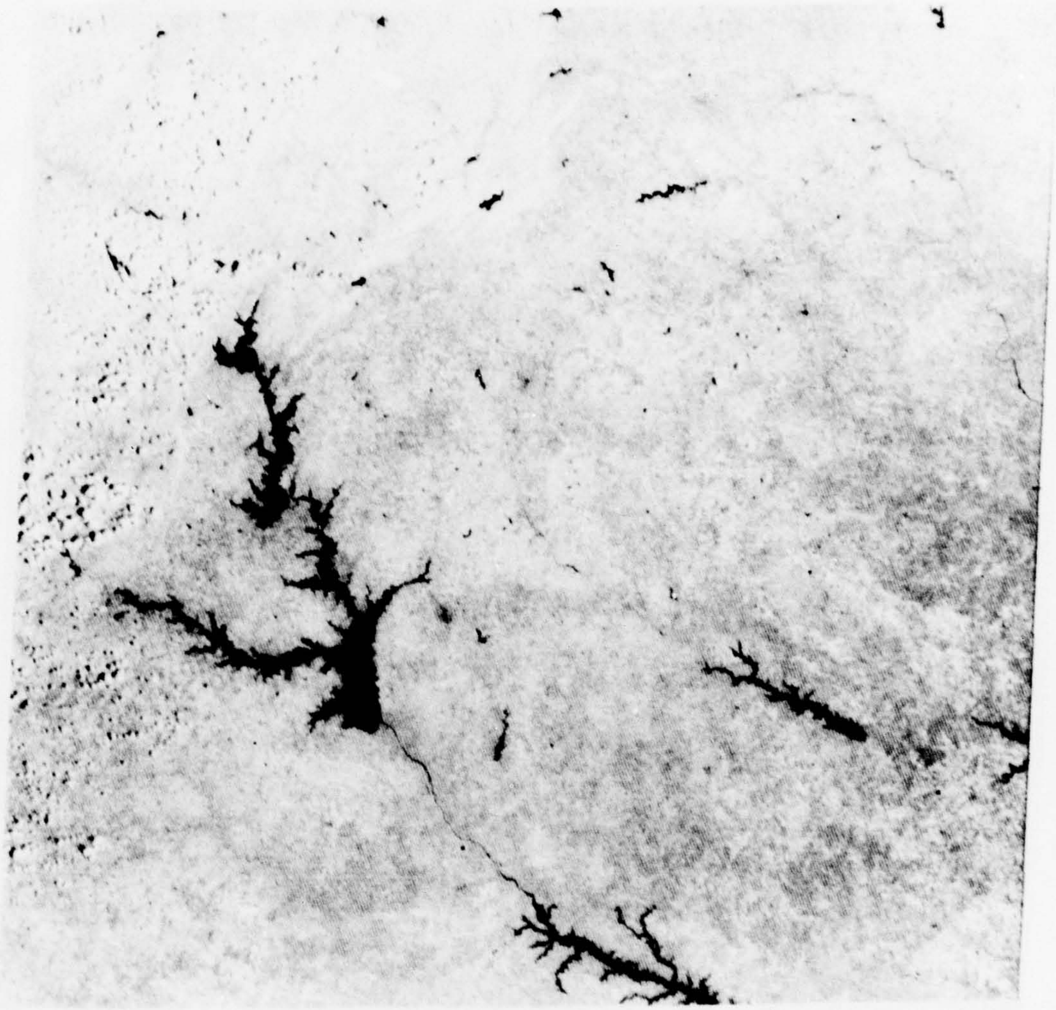

Figure 4-10 Landsat MSS-7 Image (2205-15253) at 1525 GMT on 15 August 1975. (This scene corresponds to the lower area outlined in Figure 4-8)

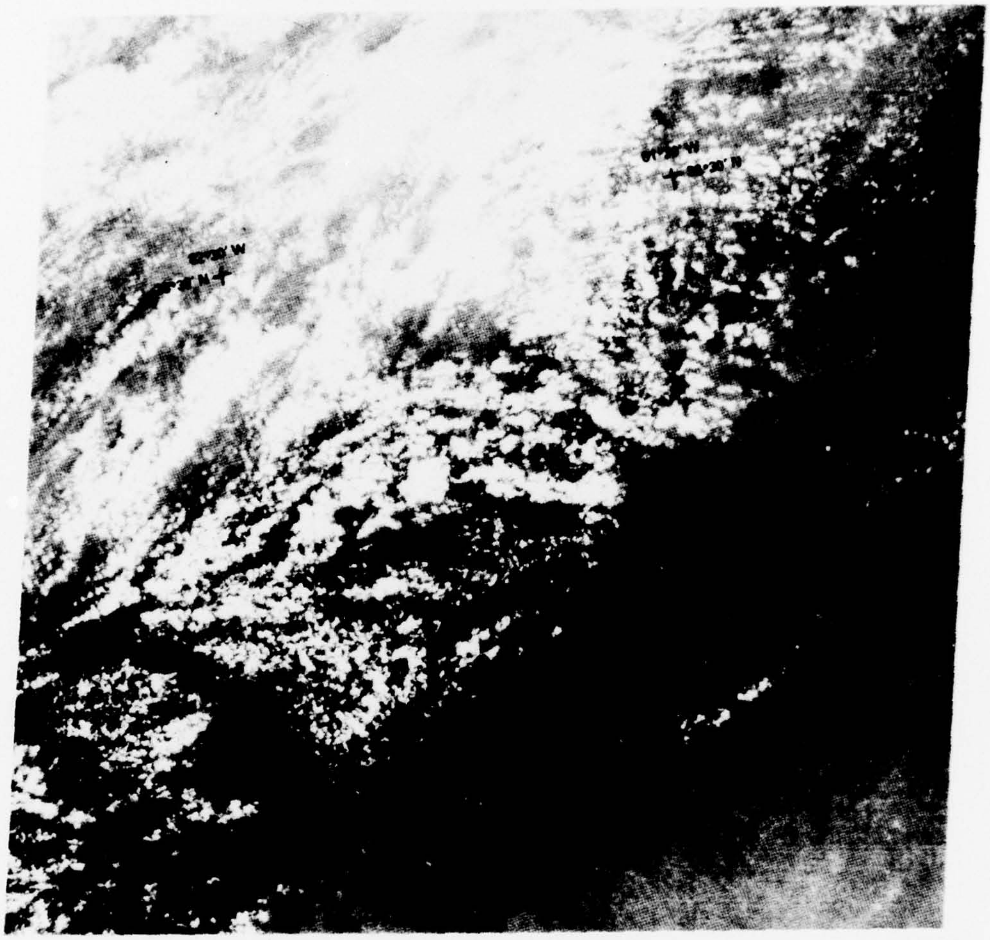

Figure 4-11 Landsat MSS-4 Image (2205-15250) at 1525 GMT on 15 August 1975. (This scene corresponds to the top area outlined in Figure 4-8)

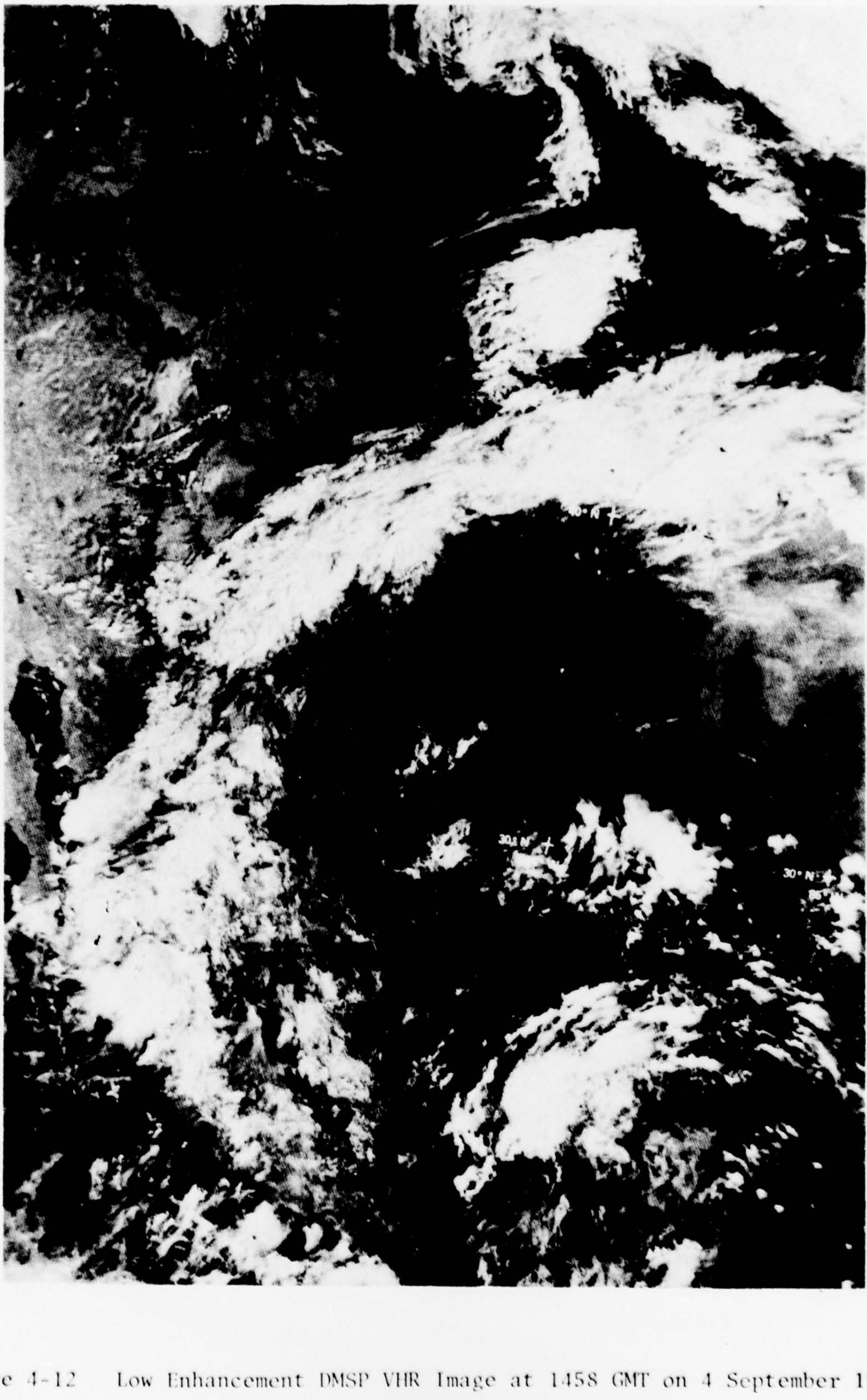

Figure 4-12 Low Enhancement DMSP VHR Image at 1458 GMT on 4 September 1975

Figure 4-13 Low Enhancement DMSP VHR Image at 1458 GMT on 4 September 1975 with Area of Correlative Landsat Imagery Outlined and 1500 GMT Surface Weather Observations Shown

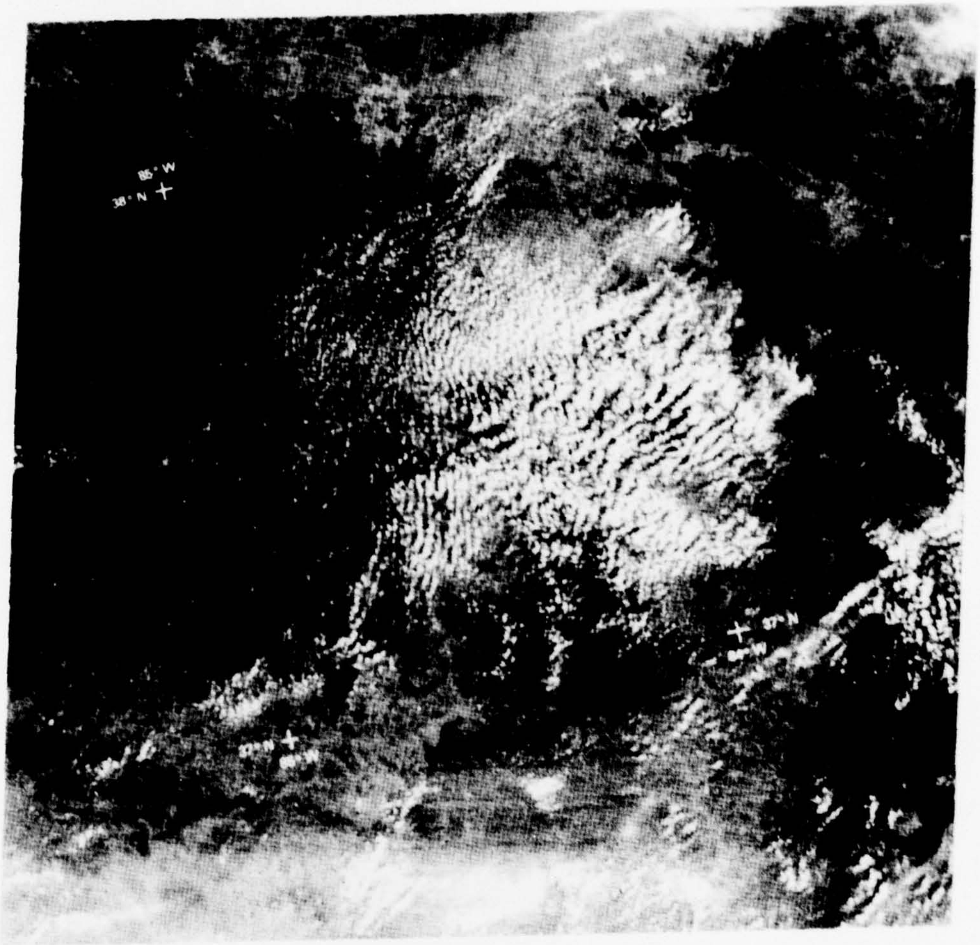

Figure 4-14 Landsat MSS-4 Image (2225-15355) at 1535 GMT on 4 September 1975. (This scene corresponds to the top area outlined in Figure 4-13)

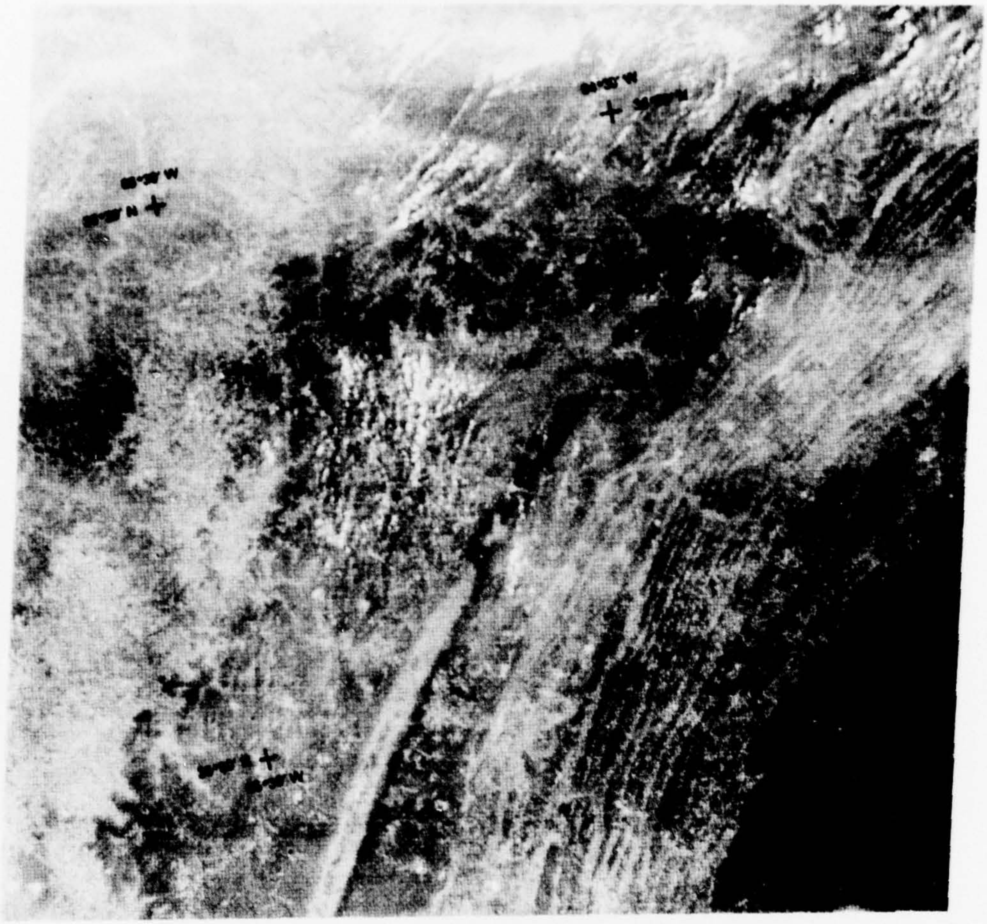

Figure 4-15 Landsat MSS-4 Image (2225-15362) at 1536 GMT on 4 September 1975. (This scene corresponds to the lower area outlined in Figure 4-13)

display an overall haziness, compared to the MSS-5, 6, and 7 bands, which appear completely haze-free (images not shown). Also, rows of small-celled cumulus clouds not observed in the lower resolution DMSP imagery are observed in the Landsat data.

The overall synoptic pattern indicated a stationary high pressure system over the entire region with calm to light southerly surface winds, considerable light fog and haze, and high humidity. At 1500 GMT, surface temperatures were generally in the 27° to 30°C range (low to mid-80s°F), with dew point temperatures generally near 21°C (70°F).

4.5 Case 5: 5 September 1975 - Mid-Atlantic Coast

A relatively broad area of anomalous gray-shade pattern over the southeastern part of the country is detectable in the low-enhancement DMSP image of 5 September 1975 (Figure 4-16). In fact, at least seven distinct gray tones can be detected within the overall DMSP anomalous gray-shade pattern (primarily over the Carolinas, near the right edge of the image). Low visibilities were reported in light fog and haze, with dew-point depressions of 1° to 3°C.

Unfortunately, the Landsat coverage on 5 September was just to the west of the most distinct anomalous gray-shade pattern in the corresponding DMSP image (the Landsat coverage is indicated in Figure 4-16). Since there was only a one-hour difference in time between the DMSP and Landsat observations, and the cloud cells seen in the DMSP image can also be seen in the center of the three Landsat scenes (Figure 4-17).

The Landsat image to the north covers the area where the DMSP image displays three distinct tonal levels. The MSS-4 band of this particular scene, shown in Figure 4-18, displays an overall haze, but no distinct variations in tone can be detected. The MSS-5 band of this scene (not shown) is less hazy, and no haziness is apparent in either the MSS-6 or 7 bands. Again, because of the variable background, it is difficult to map subtle haze patterns in the Landsat images. A difference in the overall haziness can be noted, however, in a comparison between the MSS-4 images (Figure 4-18) and the southernmost scene (Figure 4-19); the former, which is in the area of the DMSP anomalous gray-shade pattern, is considerably more hazy than the latter, which is in an area that appears clear in the DMSP image.

Figure 4-16 Low Enhancement DMSP VHR Image at 1441 GMT on 5 September 1975 with Area of Correlative Landsat Imagery Outlined and 1200 GMT Surface Weather Observations Shown

Figure 4-17 Landsat MSS-4 Image (2226-15423) at 1542 GMT on 5 September 1975. (This scene corresponds to the middle area outlined in Figure 4-16)

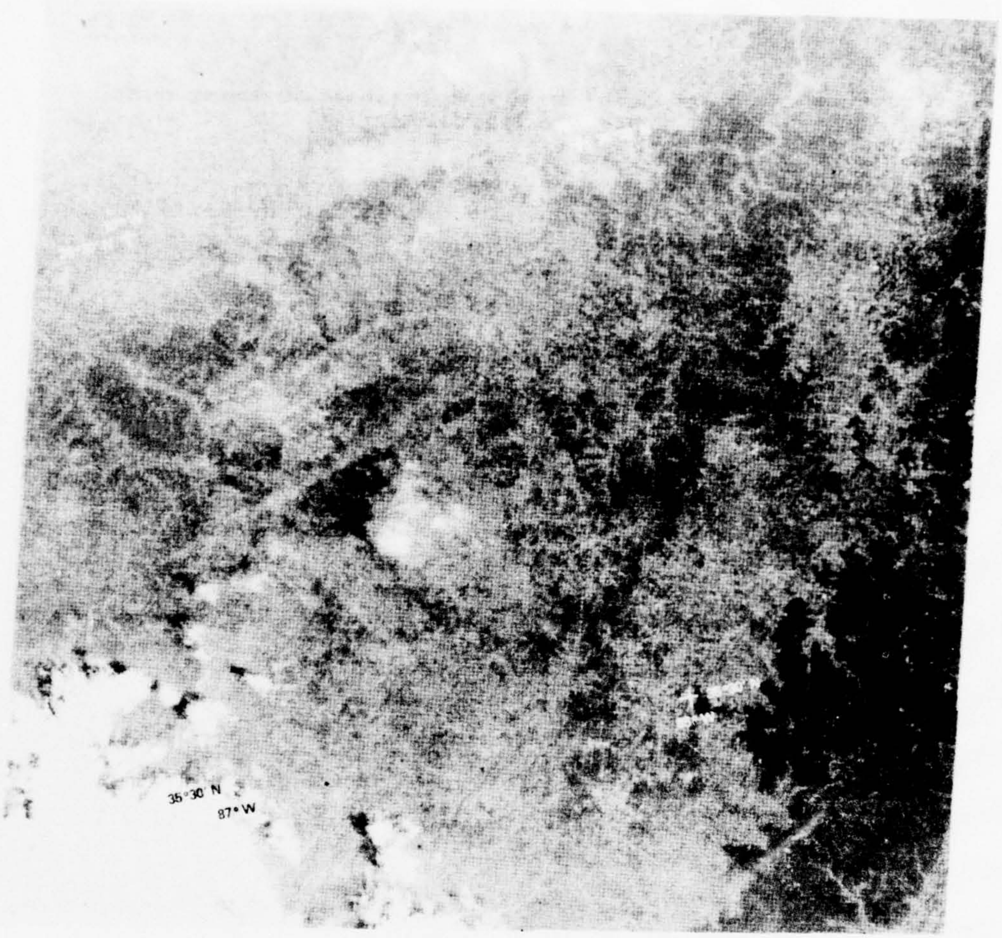

Figure 4-18 Landsat MSS-4 Image (2226-15420) at 1542 GMT on 5 September 1975. (This scene corresponds to the top area outlined in Figure 4-16)

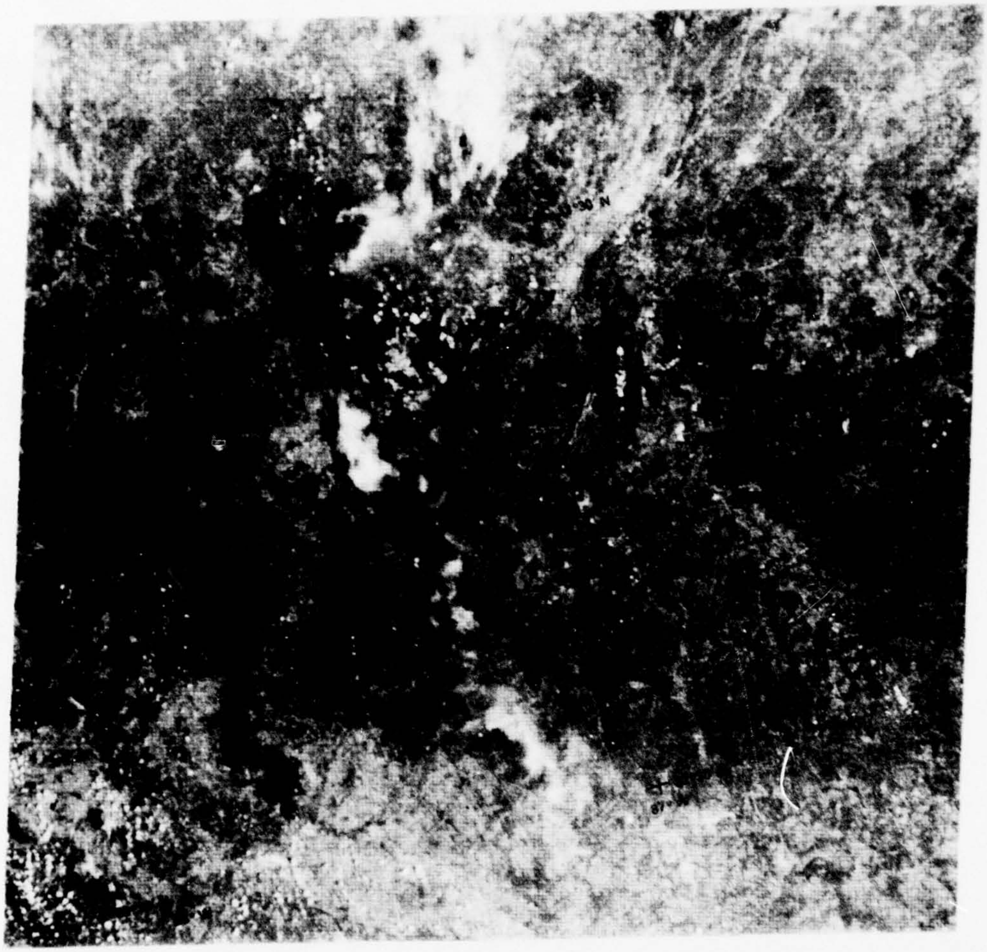

Figure 4-19 Landsat MSS-4 Image (2226-15425) at 1542 GMT on 5 September 1975. (This scene corresponds to the lower area outlined in Figure 4-16)

4.6 Case 6: 30 July 1975 - Midwestern United States (over land)

Several areas of multilayered anomalous gray shades can be detected in a low-enhancement DMSP image taken at 1412 GMT on 30 July 1975 (Figure 4-20). Although a Landsat image covers the area where there are four different tones displayed in the DMSP image, no tonal differences can be seen in any of the four Landsat spectral bands. One Landsat scene, which is over a lighter-toned anomalous gray area, shows more haziness in the MSS-4 image (Figure 4-21) than another Landsat scene that is over a darker-toned anomalous gray region; in both of these scenes, however, the MSS-5, 6, and 7 bands display no haziness. The MSS-6 image is shown in Figure 4-22. The time difference between the DMSP and Landsat observations is about 1-1/2 hours.

Examination of meteorological conditions shows that the weather systems had been relatively weak for several days with no frontal passages through the Kentucky-Ohio region. Significant weather was confined to the Gulf Coast states where showers and thunderstorms were reported. Every southern state reported dew-point temperatures of 21° to 24°C (low to mid-70s°F) on the 1200 GMT report, and this very humid air was responsible for the heavy downpours that were triggered by a weak low centered over New Orleans. The humid air extended north into Kentucky and Ohio, and there were numerous reports of restricted visibilities in fog and haze in this region.

4.7 Case 7: 7 August 1975 - Northern Italy (over land)

A low-enhancement DMSP VHR image taken at 0818 GMT on 7 August 1975 (Figure 4-23) shows a patchwork area of multilayered anomalous gray located north of Genoa in northern Italy; several other similar gray-shade patterns are scattered throughout southern Europe. Landsat imagery taken one hour after the DMSP observation, located over the area of anomalous gray shade, shows no distinct tonal variations that can be related to those seen in the DMSP image, although the MSS-4 band does appear hazy overall (Figure 4-24); the MSS-5, 6, and 7 images are clear. The MSS-6 image is shown in Figure 4-25. There were no surface weather reports available in the area where the anomalous gray-shade pattern was

Figure 4-20 Low Enhancement DMSP VHR Image at 1412 GMT on 30 July 1975 with Area of Correlative Landsat Imagery Outlined

Figure 4-21 Landsat MSS-4 Image (2189-15361) at 1536 GMT on 30 July 1975. (This scene corresponds to the lower area outlined in Figure 4-20)

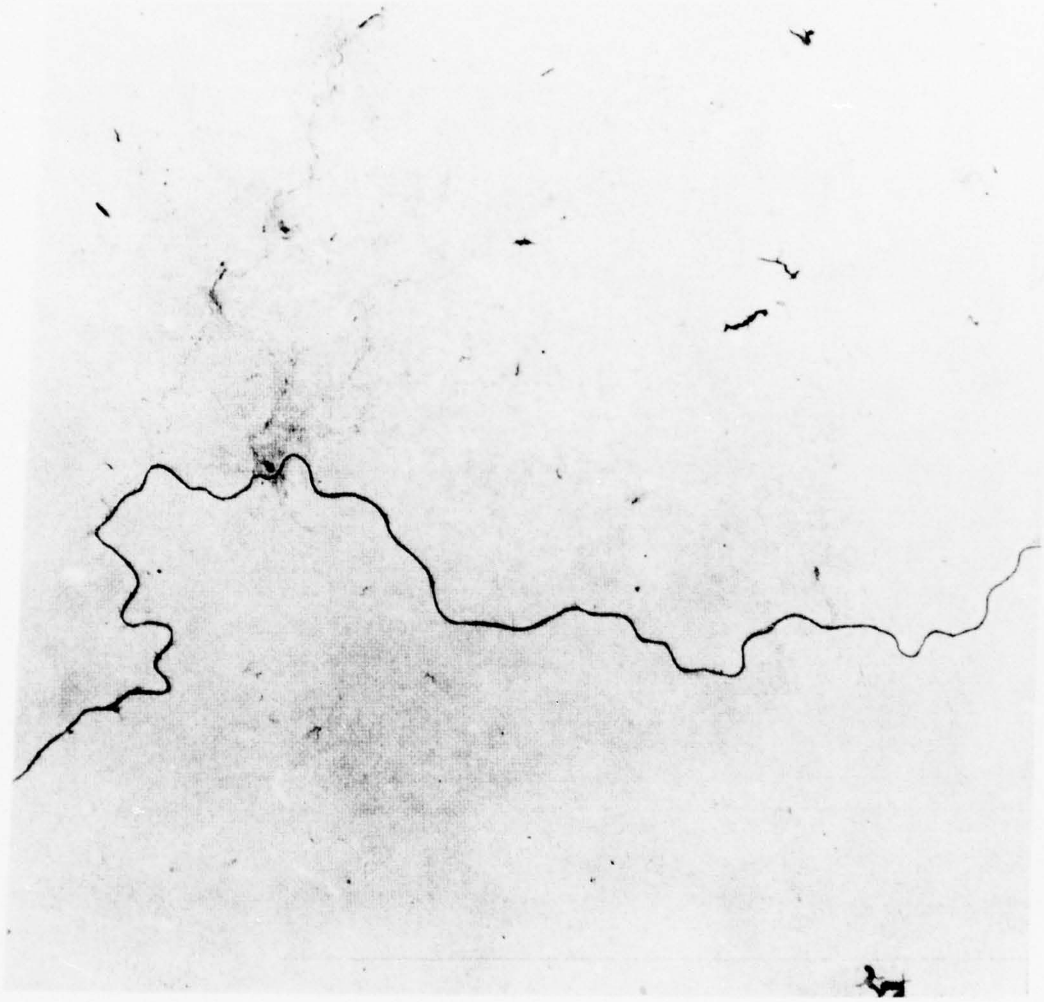

Figure 4-22 Landsat MSS-6 Image (2189-15361) at 1536 GMT on 30 July 1975

Figure 4-23 Low Enhancement DMSP VHR Image at 0818 GMT on 7 August 1975 with Area of Correlative Landsat Imagery Outlined

Figure 4-24 Mosaic of Landsat MSS-4 Images (2197-09264 and 2197-09271) at 0926 GMT on 7 August 1975

Figure 4-25 Mosaic of Landsat MSS-6 Images (2197-09264 and 2197-09271) at 0926 GMT on 7 August 1975

most intense, but just outside this area there were several reports of high humidity and restricted visibility in fog.

4.8 Case 8: 14 October 1975 - Southeastern United States (over land)

Several anomalous gray shade patterns covering a broad region of the Southeastern United States can be identified on a low-enhancement DMSP VHR image taken at 1436 GMT on 14 October 1975 (Figure 4-26). Although Landsat images were not available for this case over the region of the lightest-tone anomalous gray-shade pattern, two scenes viewing an area of darker-toned anomalous gray were available. Examination of these images again shows an overall haziness in the MSS-4 band of one of these scenes (Figure 4-27), whereas the MSS-5, 6, and 7 bands are clear. The MSS-6 image is shown in Figure 4-28. Since the Landsat observation was 1-1/2 hours after the DMSP observation, it is possible that some of the anomalous gray shade had diminished. The air over the eastern half of the United States was increasingly more stagnant during the five days prior to the date of observation, and within the general area of the DMSP anomalous gray-shade pattern, there were numerous reports on the 1200 GMT surface chart of fog and haze with moderate to high humidity.

Figure 4-26 Low Enhancement DMSP VHR Image at 1436 GMT on 14 October 1975 with Areas of Correlative Landsat Imagery Outlined

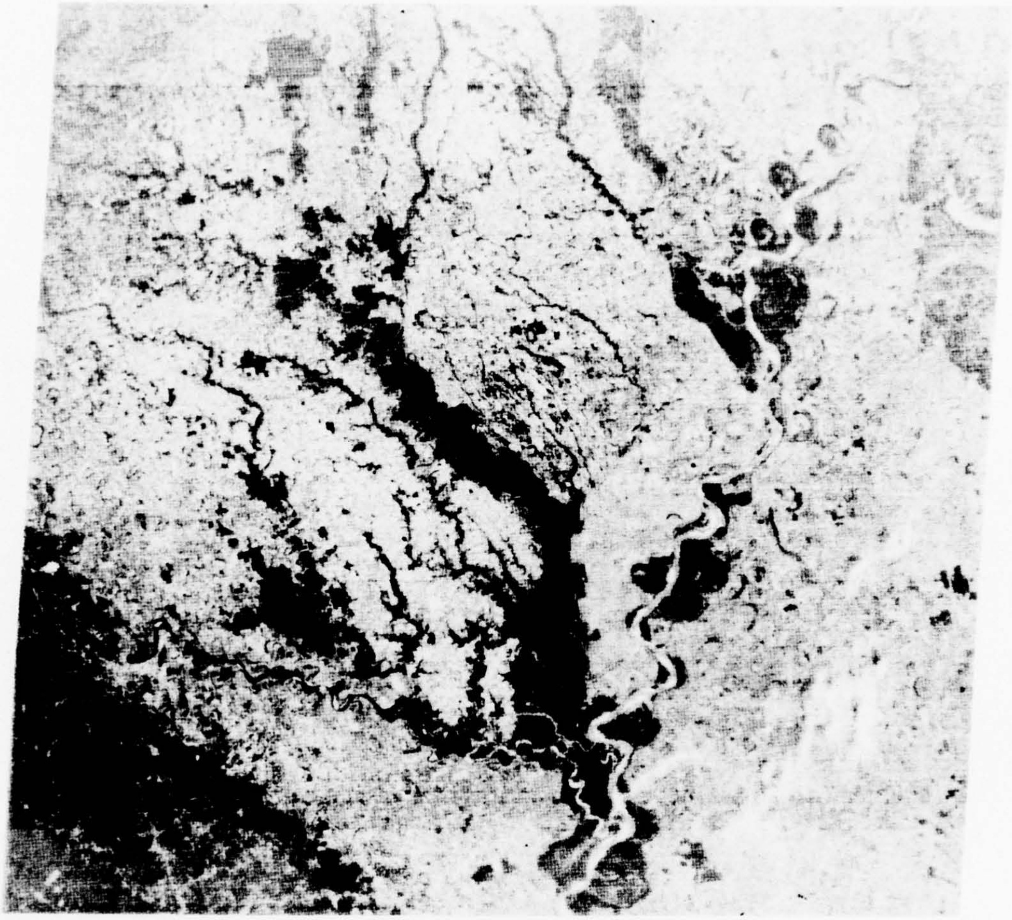

Figure 4-27 Landsat MSS-4 Image (2265-15592) at 1559 GMT on 14 October 1975. (This scene corresponds to the lower area outlined in Figure 4-26)

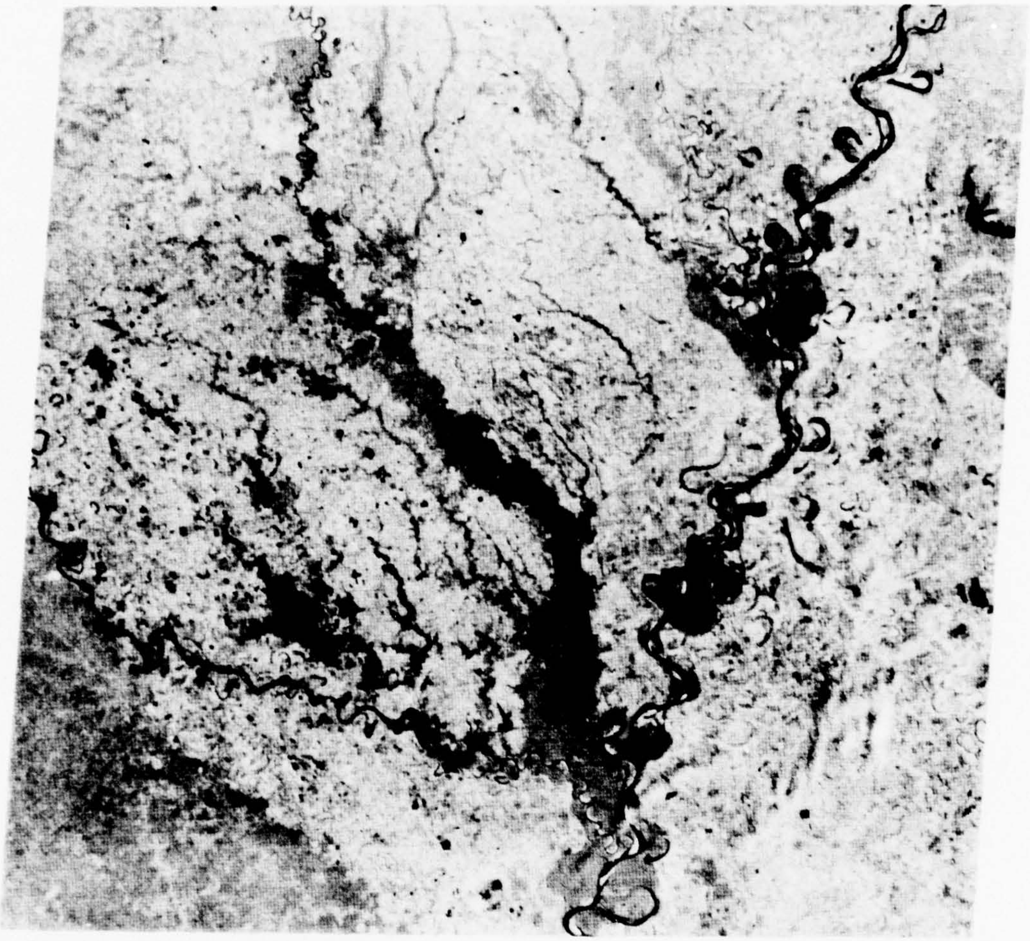

Figure 4-28 Landsat MSS-6 Image (2265-15592) at 1559 GMT on 14 October 1975

5. INVESTIGATION OF THE EFFECT OF WATER VAPOR ON VISIBLE AND NEAR-INFRARED IMAGERY

5.1 Introduction

Both the DMSP VHR and Landsat MSS instruments view a highly complex geophysical surface. As these satellite-based radiometers scan the earth scene within their respective fields of view, a multishade image of individual resolution elements or pixels is formed, each with a characteristic inherent brightness caused by the scene's areal inhomogeneity. Quantitatively, the brightness of each pixel expressed in terms of a measured intensity is dependent on a number of identifiable parameters including geometric factors (solar elevation, azimuth angles, and viewing geometry), reflecting properties of the surface (its spectral reflectivity), and the composition of the intervening atmosphere (abundances of water vapor and other absorbing gases and amounts of various particulates such as aerosol and haze).

An additional consideration with particular relevance to DMSP/Landsat data comparison is the highly structured spectral nature of the observed earth-atmosphere system. In addition to variation within the field-of-view, for example, both surface reflectance and atmospheric absorption and scattering properties are functions of the wavelength of observation. Interpretation of imagery is complicated by the difficulty of establishing a one-to-one correspondence between physical features and measured intensities when the spectral bandwidth of the sensor is wide enough to be sensitive to a variety of wavelength-dependent phenomena. Therefore, there is a spectral resolution problem in addition to the more commonly considered areal resolution problem.

In this section, a number of simple models based on radiative transfer theory are applied to the DMSP spectral interval (0.4 to 1.1 μm) to elucidate the particular interaction mechanisms prevalent at various wavelengths and to simulate mathematically the intensities that would be measured by both the DMSP VHR and Landsat MSS instruments. In particular, the cases of a relatively clear atmosphere and one with reduced visibility are compared for varying amounts of water vapor abundance.

5.2 Characteristics of Absorption and Scattering Mechanisms within the DMSP Spectral Interval

Both the DMSP VHR and the Landsat MSS are sensitive to radiation in the 0.4 to 1.1 μm wavelength region. The spectral response curves, $\phi(\lambda)$, of each of these instruments are illustrated in Figures 2-1 and 2-3, respectively (Fett and Mitchell 1977, Norwood et al. 1972). An essential feature distinguishing the two instruments is the division of the spectral interval into four distinct bands by the Landsat sensor. These bands are designated MSS-4, 5, 6, and 7, respectively. Band limits, center wavelengths, and band number are given in Table 5-1. In contrast, the DMSP VHR has one channel within the same spectral region centered at approximately 0.8 μm. Approximate response curve values are given in Table 5-2. For this reason, the Landsat instrument has a higher spectral resolution forming the basis of the DMSP/Landsat multispectral data comparison.

A variety of absorption and scattering mechanisms are active in the visible (0.4 to 0.7 μm) and near-infrared (0.7 to 1.1 μm) spectral regions. For the purpose of data comparison, they can best be characterized as either resonant or nonresonant phenomena. Resonant phenomena occur at specific, predictable wavelengths or wavelength intervals, while nonresonant phenomena have relatively smooth wavelength dependence and are broadly distributed across the spectrum. Within the 0.4 to 1.1 μm wavelength region, the primary sources of resonant opacity are the absorbing gases, including water vapor and ozone (Goody 1964), while the complementary nonresonant sources are caused by molecular (Rayleigh) scattering and Mie extinction from particulates in the form of naturally occurring hazes and aerosols of continental or marine origin (Deirmendjian 1964). Thus, in general, resonant mechanisms will affect only a portion of the DMSP spectral interval (and may be particularly significant for a given Landsat MSS band), while nonresonant mechanisms influence the entire wavelength region. For example, water vapor is more important in the near infrared while various scattering effects caused by hazes are prominent in the visible (Isaacs and Chang 1975).

TABLE 5-1

LANDSAT MSS BANDS

Landsat MSS Band	Peak Response (μm)	Center Wavelength (μm)	Wavelength Limits (μm)
4	0.530	0.55	0.50-0.60
5	0.635	0.65	0.60-0.70
6	0.730	0.75	0.70-0.80
7	0.830	0.95	0.80-1.1

TABLE 5-2

DMSP VHR RESPONSE $\phi(\lambda)$

$\lambda(\mu m)$	$\phi(\lambda)$	$\lambda(\mu m)$	$\phi(\lambda)$	$\lambda(\mu m)$	$\phi(\lambda)$
0.4000	0.0154	0.6993	0.8615	1.0101	0.4000
0.4082	0.0308	0.7092	0.8769	1.0309	0.3231
0.4167	0.0577	0.7194	0.9000	1.0526	0.2615
0.4255	0.0846	0.7299	0.9077	1.0753	0.1846
0.4348	0.1077	0.7407	0.9308	1.0989	0.1077
0.4444	0.1308	0.7519	0.9462		
0.4545	0.1615	0.7634	0.9615		
0.4651	0.2000	0.7752	0.9692		
0.4762	0.2310	0.7874	0.9769		
0.4878	0.2538	0.8000	0.9846		
0.5000	0.2923	0.8130	0.9923		
0.5128	0.3308	0.8264	0.9769		
0.5263	0.3692	0.8403	0.9615		
0.5405	0.4308	0.8547	0.9462		
0.5556	0.4620	0.8696	0.9230		
0.5714	0.5000	0.8850	0.8769		
0.5882	0.5615	0.9009	0.8231		
0.6061	0.6231	0.9174	0.7538		
0.6250	0.6920	0.9346	0.5538		
0.6452	0.7385	0.9524	0.6308		
0.6667	0.8000	0.9709	0.5000		
0.6897	0.8384	0.9901	0.4692		

The wavelength dependence of these separate contributions to the total atmospheric transmittance from the surface to space, $T(\lambda)$, is shown in Figure 5-1a through 5-1e. The quantity determining the ratio of incident intensity to transmitted intensity at the surface is the total atmospheric optical depth, τ^*, a highly wavelength dependent dimensionless parameter given by:

$$\tau^*(\lambda) \;=\; \sum_i \tau_i^*(\lambda) \;=\; \sum_i \int_0^\infty n_i(z)\,[\sigma_i(\lambda) + k_i(\lambda)]\,dz \qquad (5\text{-}1)$$

where

$\tau_i^*(\lambda)$ is the optical depth due to absorber or scatterer, i

$n_i(z)$ is the number density profile for absorber or scatterer, i (cm^{-3})

$\sigma_i(\lambda)$ is the wavelength dependent scattering cross section for scatterer, i (cm^2)

$k_i(\lambda)$ is the wavelength dependent absorption cross section for absorber, i (cm^2)

The integration extends from the surface to space. An incident beam of radiation at the top of the atmosphere of wavelength, λ, will be attenuated by a factor equal to the transmittance, $T(\lambda)$:

$$T(\lambda) \;=\; \exp\,(-\sum_i \tau_i^*) \;=\; \prod_i \exp\,(-\tau_i^*) \qquad (5\text{-}2)$$

Plotted in Figure 5-1 (a)(d) are individual contributions to the total transmissivity caused by molecular scattering; aerosol extinction; ozone, carbon dioxide, nitrogen dioxide, CH_4, and so forth; and water vapor. Since the optical depths are additive, the transmissivities multiply to yield the total for the atmosphere (e). Calculations were performed using computer code LOWTRAN 2 (Selby and McClatchey 1972) for a tropical atmosphere with relative humidity of about 80% at the surface. A surface visibility of 23 km is assumed (that is, the aerosol extinction at 0.55 μm is 0.158 km^{-1}). The model atmosphere used in the computation is given in Table 5-3.

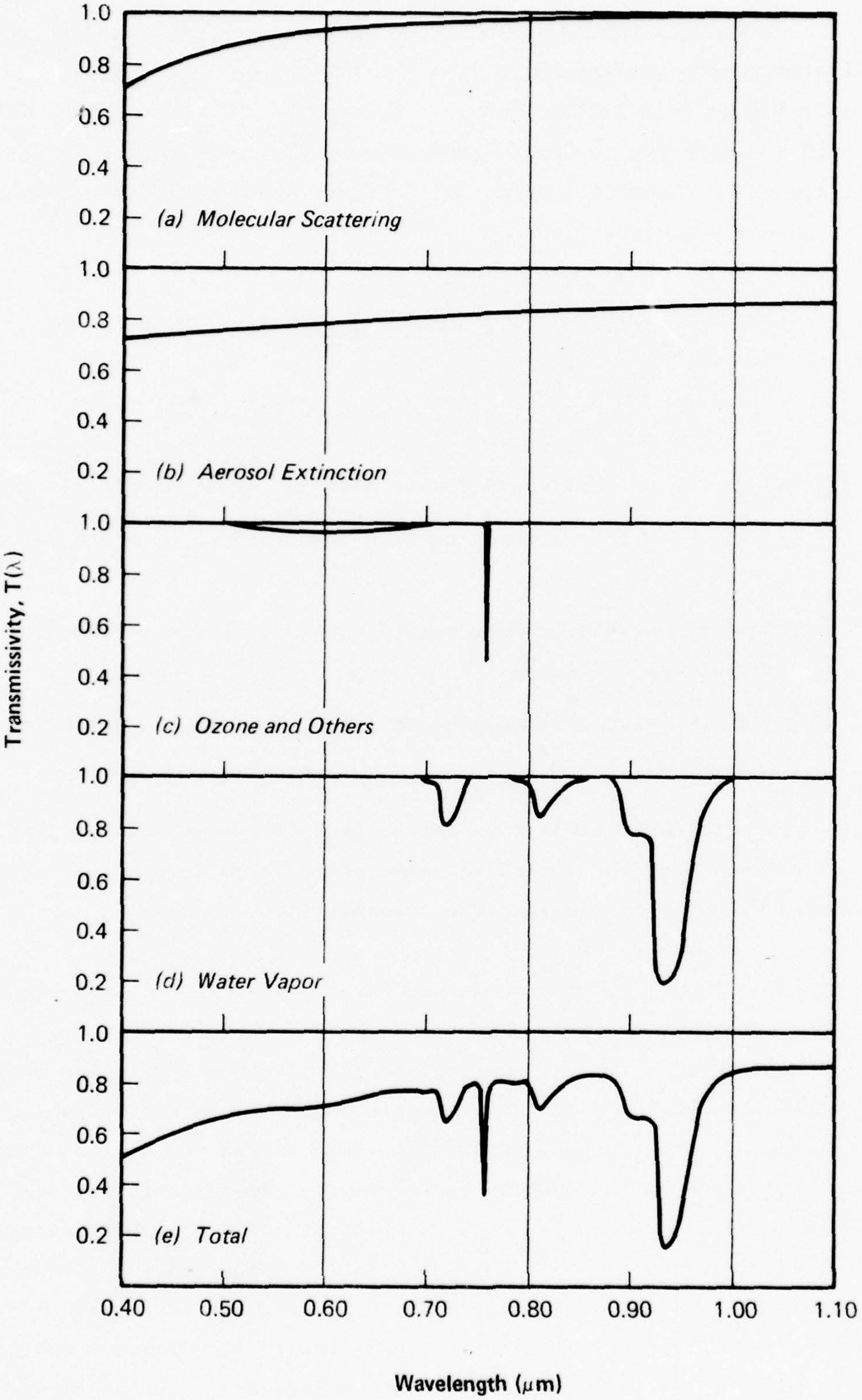

Figure 5-1 Separate Extinction Contributions in the 0.4 to 1.1 μm Spectral Region

TABLE 5-3

MODEL ATMOSPHERE USED AS A BASIS OF THE COMPUTATION OF ATMOSPHERIC OPTICAL PROPERTIES

TROPICAL

Ht. (km)	Pressure (mb)	Temp. (^oK)	Density (g/m^3)	Water Vapor (g/m^3)	Ozone (g/m^3)
0	1.013E+03	300.0	1.167E+03	1.9E+01	5.6E-05
1	9.040E+02	294.0	1.064E+03	1.3E+01	5.6E-05
2	8.050E+02	288.0	9.689E+02	9.3E+00	5.4E-05
3	7.150E+02	284.0	8.756E+02	4.7E+00	5.1E-05
4	6.330E+02	277.0	7.951E+02	2.2E+00	4.7E-05
5	5.590E+02	270.0	7.199E+02	1.5E+00	4.5E-05
6	4.920E+02	264.0	6.501E+02	8.5E-01	4.3E-05
7	4.320E+02	257.0	5.855E+02	4.7E-01	4.1E-05
8	3.780E+02	250.0	5.258E+02	2.5E-01	3.9E-05
9	3.290E+02	244.0	4.708E+02	1.2E-01	3.9E-05
10	2.860E+02	237.0	4.202E+02	5.0E-02	3.9E-05
11	2.470E+02	230.0	3.740E+02	1.7E-02	4.1E-05
12	2.130E+02	224.0	3.316E+02	6.0E-03	4.3E-05
13	1.820E+02	217.0	2.929E+02	1.8E-03	4.5E-05
14	1.560E+02	210.0	2.578E+02	1.0E-03	4.5E-05
15	1.320E+02	204.0	2.260E+02	7.6E-04	4.7E-05
16	1.110E+02	197.0	1.972E+02	6.4E-04	4.7E-05
17	9.370E+01	195.0	1.676E+02	5.6E-04	6.9E-05
18	7.890E+01	199.0	1.382E+02	5.0E-04	9.0E-05
19	6.660E+01	203.0	1.145E+02	4.9E-04	1.4E-04
20	5.650E+01	207.0	9.515E+01	4.5E-04	1.9E-04
21	4.800E+01	211.0	7.938E+01	5.1E-04	2.4E-04
22	4.090E+01	215.0	6.645E+01	5.1E-04	2.8E-04
23	3.500E+01	217.0	5.618E+01	5.4E-04	3.2E-04
24	3.000E+01	219.0	4.763E+01	6.0E-04	3.4E-04
25	2.570E+01	221.0	4.045E+01	6.7E-04	3.4E-04
30	1.220E+01	232.0	1.831E+01	3.6E-04	2.4E-04
35	6.000E+00	243.0	8.600E+00	1.1E-04	9.2E-05
40	3.050E+00	254.0	4.181E+00	4.3E-05	4.1E-05
45	1.590E+00	265.0	2.097E+00	1.9E-05	1.3E-05
50	8.540E-01	270.0	1.101E+00	6.3E-06	4.3E-06
70	5.790E-02	219.0	9.210E-02	1.4E-07	8.6E-08
100	3.000E-04	210.0	5.000E-04	1.0E-09	4.3E-11

Source: Selby and McClatchey (1972)

On examining Figure 5-1, the difference in spectral dependence between the nonresonant (a and b) and resonant (c and d) extinction mechanisms is immediately apparent. The scattering coefficient for molecular scattering, β_r (cm^{-1}), closely follows the familiar λ^{-4} Rayleigh scattering law (with a slight departure owing to the wavelength dependence of the index of refraction of air). At sea level (p = 1013 mb) for the cited model atmosphere (McClatchey et al. 1972):

$$\beta_r (\lambda) = \sigma_r (z = 0)\, n\, (z = 0) \cong 1.0922856 \times 10^{-7} \lambda^{-4.0117} \qquad (5\text{-}3)$$

The corresponding sharp decrease in atmospheric transmissivity toward shorter wavelength can be seen in Figure 5-1(a).

The situation is somewhat more complex for aerosol extinction. The optical properties of the specific aerosol or haze encountered depend on its chemical composition (characterized by its complex index of refraction) and the size ranges of particles present. Analytically, the extinction coefficient for a distribution of aerosol particles is given by:

$$\beta_a(\lambda) = \int_0^\infty \Pi r^2 Q_e (\tilde{m}, r, \lambda)\, n\, (r)\, dr \qquad (5\text{-}4)$$

where

r is the radius of the particulate

$\tilde{m}$ is the complex index of refraction

Q_e is the Mie theory (1908) efficiency factor for extinction

$n(r)$ is the number of particles per unit volume between size ranges r and $r + dr$.

Similar expressions exist for the aerosol scattering and absorption coefficients with $Q_e = Q_s + Q_a$. The Mie efficiency factors (van de Hulst 1957) are complicated functions of the particle complex index of refraction and a dimensionless parameter, $\alpha = 2\pi r/\lambda$, sometimes called the Mie parameter. Figure 5-2 illustrates the oscillatory behavior of

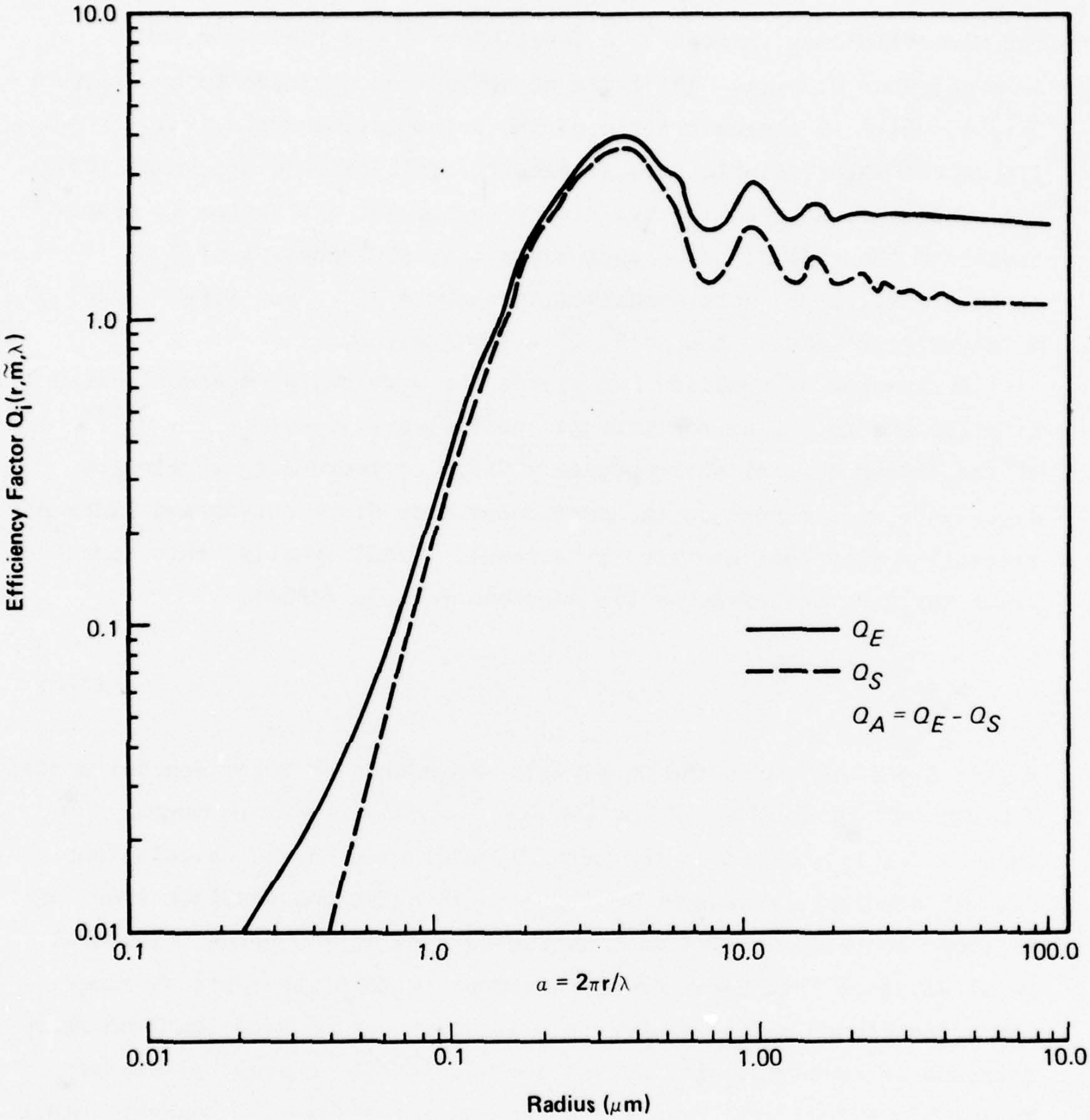

Figure 5-2 Mie Extinction Efficiency Factors

the Mie efficiency factors as a function of α and radius, r, at a wavelength of 0.55 μm. The index of refraction is taken to be 1.500 to 0.02 i, which is characteristic of the accumulation range ($0.1 \leq r \leq 1.0$ μm) of water-soluble aerosol material (Willeke and Brockmann 1977). For small values of α, the efficiency factor for extinction is proportional to the radius. As α approaches 1.0, the behavior of $Q_{e,s}$ becomes oscillatory with a maximum at about $\alpha = 4$. For large values of α, asymototic values of $Q_e = 2$, $Q_s = 1$ are reached.

Evaluation of Equation 5-2 yields the wavelength dependent extinction (or absorption or scattering) coefficients ($\beta_a = \beta_a^{abs} + \beta_a^{scatt}$) of the chosen aerosol distribution. Their corresponding wavelength dependence will depend on the particular size distribution and index of refraction that characterize the aerosol. Traditionally, this dependence has been described by the Ångström formula (1929):

$$\beta_a(\lambda) = C\lambda^{-\beta} \qquad (5\text{-}5)$$

Figure 5-3 illustrates the wavelength dependence of three aerosol models (Shettle and Fenn 1976) within the 0.4 to 1.1 μm spectral range. The rural model is closest to the aerosol model used in the calculations described below. Measurements support (Ahlquist and Charlson 1969) an Ångström coefficient of 2 and, as can be seen in the graph, the rural model displays this behavior approximately within the spectral range. Comparing Figure 5-1(b) to Figure 5-1(a), it can be seen that the sharp decrease of transmissivity at smaller wavelengths characteristic of Rayleigh scattering is greatly suppressed for aerosols. However, since Rayleigh scattering decreases much faster at longer wavelengths, the effect of aerosols is much more important at longer wavelengths (e.g., in the near infrared) than molecular scattering.

The effects on transmissivity from ozone and the uniformly mixed gases are shown in Figure 5-1(c). The Chappuis bands of ozone lie between 0.45 and 0.74 μm in the visible spectrum. The maximum absorption cross section for these bands (at about 0.60 μm) is 5×10^{-21} cm^2. An integrated ozone column of 1.068×10^{19} cm^{-2} gives an optical depth of 0.0534, or equivalently, a transmissivity of about 0.95. The effect of ozone on remote sensing of the surface is therefore negligible, although heating

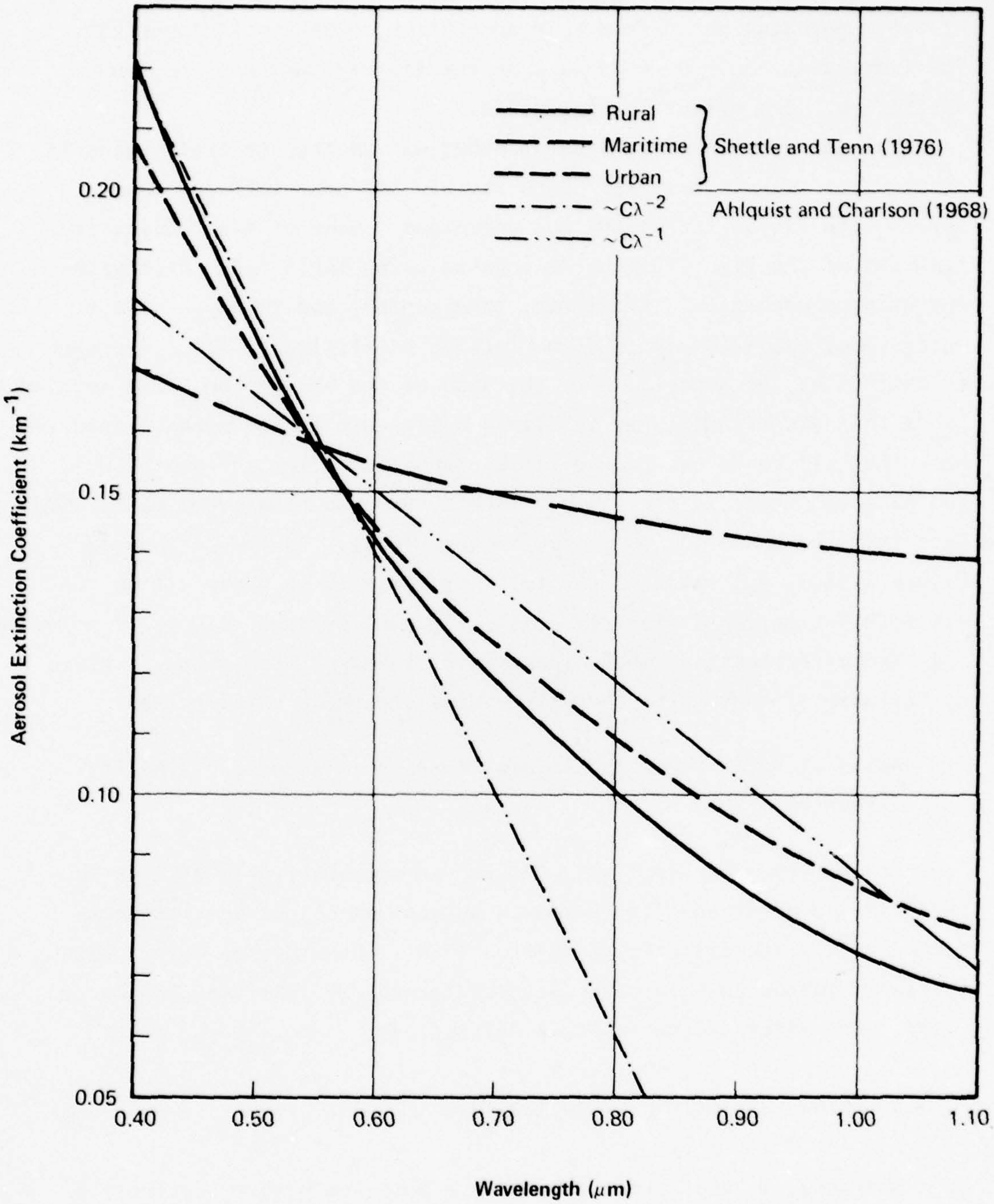

Figure 5-3 Wavelength Dependence of Aerosol Extinction Coefficient for Three Models

of the upper atmosphere from this absorption mechanism is important. The feature at about 0.76 μm is a narrow feature caused by oxygen absorption. Its effect is negligible.

The most prominent gaseous absorber within the spectral region is water vapor [Figure 5-1(d)]. Both visible and near-infrared bands appear with varying strengths and positions. Some of the qualitative features of the figure can be delineated using Table 5-4, which gives the quantum mechanical transition, band center, and strength of the water vapor bands (Goody 1964; McClatchey et al. 1973). (The strength is defined as the integral over the band of the absorption cross section.) Bands that are identifiable in Figure 5-1(d) are marked with an asterisk. Note that all bands are ground-state transitions (initial state 000), and although those in the visible (< 0.70 μm) are relatively weak, the near-infrared bands (ρ, σ, τ) are rather strong. As can be seen in Figure 5-1(e), the shape of the total transmissivity curve within the 0.4 to 0.7 μ region is largely defined by the combined effects of molecular and aerosol extinction, while in the near infrared, the shape is given by the aerosol curve with the water-vapor structure superimposed.

5.3 Roles of Water Vapor and Aerosol Amounts in Reduced Visibility Situations

Visibility is subjectively defined as the observer's ability to perceive the difference in luminance between an object and its background at a given distance (Middleton 1958). Consider an object with intrinsic luminance $B_0(0)$ against a background of intrinsic luminance $B_b(0)$. The intrinsic contrast is defined as:

$$C(0) = [B_0(0) - B_b(0)]/B_b(0) \tag{5-6}$$

At a distance, r, the apparent luminance modified both by extinction reduction and scattering sources is (Duntley 1948):

$$\begin{aligned} B_{o,b}(r) &= B_a\,[1 - \exp(-\beta r)] \\ &\quad + B_{0,b}(0) \exp(-\beta r) \end{aligned} \tag{5-7}$$

TABLE 5-4

VISIBLE AND NEAR INFRARED WATER VAPOR BANDS

	Transition	Band Center (μm)	Strength (cm)
	000-411	0.544	2×10^{-23}
	000-203	0.572	1×10^{-22}
	000-401	0.592	3×10^{-22}
	000-302	0.592	3×10^{-23}
	000-321	0.594	2×10^{-22}
	000-113	0.632	2×10^{-23}
	000-311	0.652	2×10^{-22}
	000-103	0.698	1×10^{-21}*
	000-400	0.703	1×10^{-22}
	000-301	0.723	3×10^{-21}*
	000-202	0.723	$<2 \times 10^{-23}$
	000-221	0.734	6×10^{-21}*
	000-013	0.796	1×10^{-22}
	000-112	0.806	6×10^{-21}*
	000-211	0.823	6×10^{-23}*
	000-210	0.824	1×10^{-22}*
	000-131	0.847	2×10^{-21}*
ρ	000-003	0.906	2×10^{-21}*
	000-102	0.920	4×10^{-22}*
σ	000-201	0.942	1×10^{-20}*
	000-300	0.943	6×10^{-22}*
τ	000-121	0.968	2×10^{-21}*
	000-220	0.972	$<4 \times 10^{-23}$
	000-041	1.016	4.8×10^{-23}
ϕ	000-012	1.111	1.2×10^{-21}
	000-121	1.135	5×10^{-20}

where

β^{-1} is a characteristic extinction length

B_a is a function of solar zenith and azimuth and atmospheric scattering properties

Equation 5-7 may be thought of as a simplified solution to radiative transfer along a horizontal surface sight path. The apparent contrast at distance r is then:

$$C(r) = C(0)\,\frac{B_b(0)}{B_b(r)}\,\exp(-\beta r) \tag{5-8}$$

For viewing against the horizon, $B_b(0) = B_b(r)$ and Equation 5-7 become:

$$C(r) = C(0)\,\exp(-\beta r) \tag{5-9}$$

Standard visibility is defined as that distance where the threshold of contrast perception of the average human eye is reached for a large black object against the horizon. For a black object, $C(0) = -1.0$. Extensive investigations have indicated that although contrast threshold is a strong function of object size and illumination, the value reaches a limit of ±0.02 for large, well-illuminated objects. From Equation 5-9, visibility (visual range) in kilometers is (Koschmieder 1924):

$$V = -\frac{\ln(0.02)}{\beta} = \frac{3.912}{\beta} \tag{5-10}$$

where

β is the total extinction coefficient (km^{-1}) at 0.55 μm (peak spectral response of human photopic vision)

Visibility, therefore, is largely determined by optical properties at 0.55 μm. From the discussion in the previous section, it would appear that molecular scattering and aerosol extinction would be largely responsible for reducing visibility.

To investigate the relative effects of varying water vapor and aerosol amounts on the entire spectral interval (0.4 to 1.1 μm), model atmosphere calculations of the transmissivity spectrum analogous to Figure 5-1(e) were generated using the LOWTRAN 2 program for three water vapor amounts and two visibilities. Assumed integrated water vapor amounts were: 3.35 g/cm^2, 0.335 g/cm^2, and 0.0335 g/cm^2. These values correspond to surface relative humidities of approximately 80%, 8%, and 0.8%, respectively, for the tropical atmosphere used. The aerosol amount was determined by the visibility at 0.55 μm. The two models selected were 23 km (relatively clear) and 5 km (hazy). They correspond to aerosol extinction coefficients of 0.158 km^{-1} and 0.7704 km^{-1}, respectively, assuming a molecular scattering contribution of 0.012 km^{-1}. The reduced visibility case (5 km) represents an increase in the number density of scatterers by a factor of almost 5, assuming the shape of the size distribution [n(r)] remains constant (only approximately true).

The effect of decreasing the water vapor amount by factors of 10 is illustrated in Figure 5-4. As water vapor amount decreases, the predominant effects are experienced at the near-infrared wavelengths where transmissivity increases as water vapor (relative humidity) decreases. Conversely, in Figure 5-5, the relative humidity is maintained at 80%, while the visibility is decreased from 23 to 5 km (aerosol loading increased by factor of about 5). Here the transmissivity is reduced across the entire spectrum (the effect is greatest at shorter wavelengths) with the water vapor influence remaining essentially the same. When water vapor is removed from a hazy atmosphere (Figure 5-6), once again the predominant effect is in the near infrared, where transmissivity increases. Three conclusions can be drawn from these calculations: (1) changes in relative humidity affect only the spectral regions where water vapor bands are present such as the near infrared, (2) changes in aerosol amount primarily affect the complimentary spectral regions, and (3) the effect of aerosols is dominant.

It should be noted, however, that in a realistic atmosphere, variations of humidity and visibility are not independent. Qualitatively, high humidities should associate with reduced visibilities and vice versa. Empirically, it has been demonstrated that the extinction caused

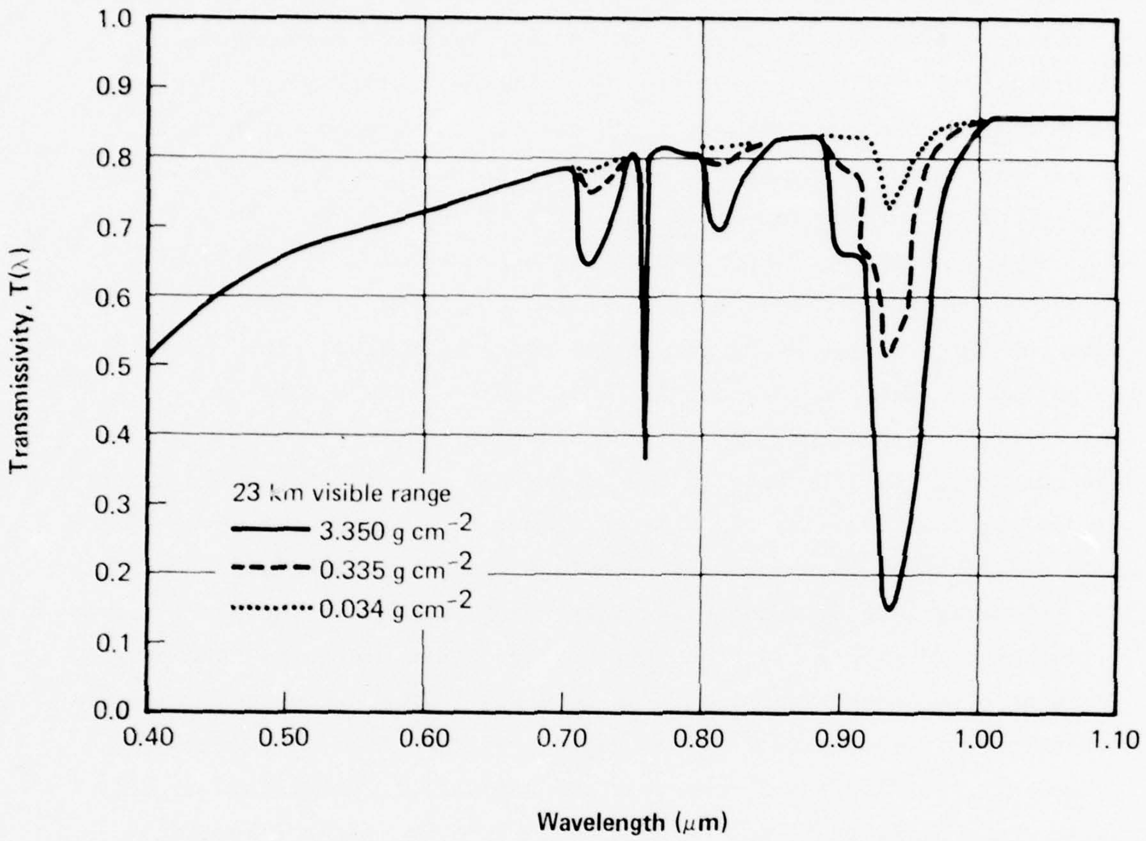

Figure 5-4 Effect of Decreasing Water Vapor Amount in Relatively Clear Atmosphere

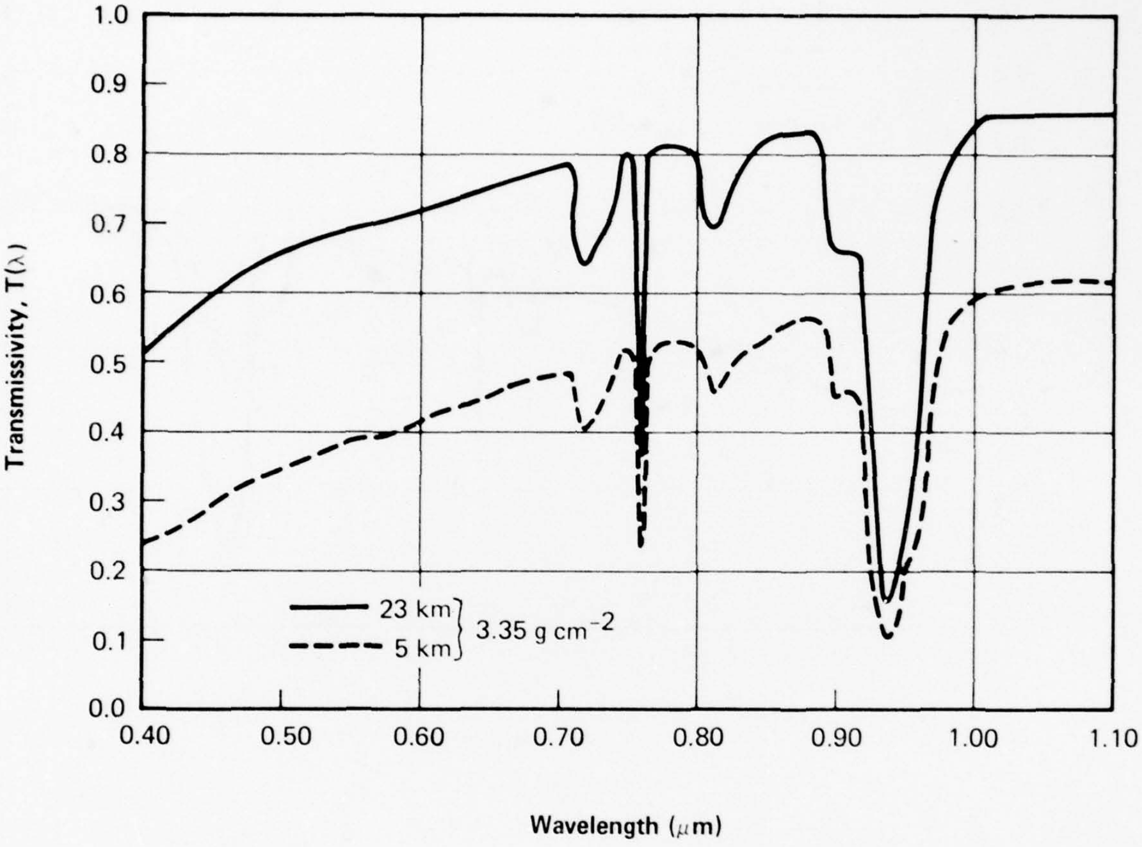

Figure 5-5 Effect of Increasing Aerosol Amount for Constant Humidity Atmosphere (80%)

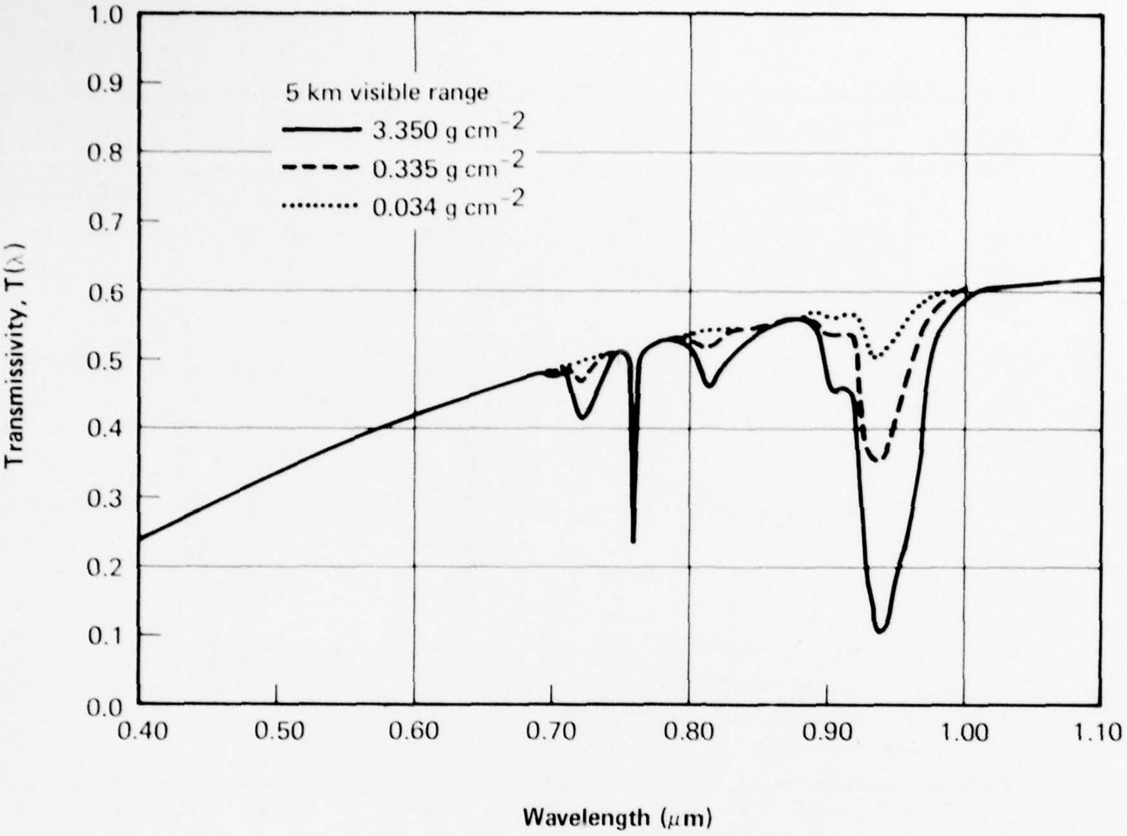

Figure 5-6 Effect of Decreasing Water Vapor Amount in Hazy Atmosphere

by certain aerosols increases with increased humidity either monotonically or drastically after a specific threshold (usually $\sim$75% relative humidity). This finding implies a corresponding decrease of visual range with increasing humidity. The mechanism accounting for this correlation is the growth of haze droplets within the optically active size range (0.1 to 1.0 μm) (Pueschel and Noll 1967). It has been shown that the aerosol extinction coefficient correlates well with the mass of aerosol within this size range (Hidy 1975). Therefore, a more realistic comparison would be between the low humidity curves for the 23-km visual range (Figure 5-4) and the high humidity curve in Figure 5-6. Since aerosol growth mechanisms have not been modeled, no attempt has been made to obtain a self-consistent water vapor abundance/aerosol loading relationship.

5.4 Simulation of Satellite Sensor Radiances - Radiative Transfer Analysis

In the previous section, the sensitivity of the earth's transmissivity spectrum to variations of aerosol and water vapor abundance was examined for the spectral interval 0.4 to 1.1 μm encompassing the response functions of the DMSP VHR and Landsat MSS sensors. In this section, a radiative transfer analysis technique is described that is used to simulate radiances measured by these satellite-based sensors. This theoretical analysis provides the basis for a discussion of the relative impact of water vapor and aerosol on each of the Landsat MSS bands in addition to comparison with the DMSP VHR.

5.4.1 Radiative Transfer Theory

The radiative transfer equation for a plane parallel atmosphere is given by:

$$\mu \frac{dI_\lambda}{d\tau_\lambda} = I_\lambda - J_\lambda \tag{5-11}$$

where

I_λ is the specific intensity of radiation at wavelength, λ (ergs $\mathrm{cm}^{-2}\mathrm{sec}^{-1}\mathrm{str}^{-1}\ \mu\mathrm{m}^{-1}$)

J_λ is the source function at wavelength, λ

μ is the cosine of the zenith angle of observation

τ_λ is the optical depth at wavelength, λ

For an atmosphere with both absorption and scattering, the optical depth at wavelength, λ, and altitude, z, is given by (see Equation 5-1):

$$\tau_\lambda(z) = \sum_i \int_z^\infty n_i(z)[\tau_i(\lambda) + k_i(\lambda)]\, dz \qquad (5\text{-}12)$$

For illumination by the sun with no thermal source function and assuming both azimuthal symmetry (no dependence on sun azimuth) and isotropic scattering, the source function is given by:

$$J_\lambda(\tau,\mu) = \frac{\omega_o(\tau)F}{4}\, e^{-\tau/\mu_o} + \frac{\omega_o(\tau)}{2} \int_{-1}^{+1} I_\lambda(\tau,\mu')\, d\mu' \qquad (5\text{-}13)$$

where πF is the wavelength dependent incident solar flux and μ_o is the cosine of the solar zenith angle. The quantity $\omega_o(\tau)$ is the wavelength-dependent single scattering albedo defined as the ratio of the total scattering coefficient at optical depth, τ, to the total extinction coefficient at optical depth, τ, or:

$$\omega_o[\tau(z)] = \frac{\sum_i n_i(z)\ \sigma_i(\lambda)}{\sum_i n_i(z)[\sigma_i(\lambda) + k_i\ (\lambda)]} \qquad (5\text{-}14)$$

Values of the single scattering albedo range from 0.0 for pure absorption to 1.0 for pure scattering.

The assumptions of azimuthal symmetry and isotropic scattering are somewhat restrictive and require further discussion. It is well known that the angular scattering (phase) function of combined molecular and aerosol scattering is not isotropic; on the contrary, it is strongly forward peaked (Deirmendjian 1964). The effect of this anisotropy in comparison to the assumed isotropic analysis depends on the sun's elevation and azimuth. For the sun directly overhead ($\mu_o = 1.0$), symmetry with respect to azimuth angle is maintained, and the assumption of isotropy implies an overestimation of calculated radiances for high and moderate observation angles owing to the predominance of forward to back scattering for the actual aerosol distribution (Kattawer and Plass 1968). When the sun is not at zenith (as is most often the case), the radiances are not symmetric with the azimuth angle, and the assumption of isotropy overestimates their magnitudes in the antisolar direction and underestimates them in the solar direction. Since the effect of spectral differences is sought, a particular viewing geometry and isotropic scattering has been assumed in this first-order analysis. A more detailed analysis should account for the relative solar azimuth and scan geometry within the field of view and the effects of anisotropy.

Assuming a Lambertian surface (the upward reflected intensity is independent of observation angle), the source function $J(\tau)$ allows the following integral equation:

$$
\begin{aligned}
J(\tau) = {} & \frac{\omega_o(\tau)}{4} F \exp(-\tau/\mu_o) \\
& + \frac{\omega_o(\tau)}{4} \int_o^{\tau^*} J(\tau)\, E_1(|t-\tau|)\, dt \\
& + \omega_o(\tau)\, r\, E_2(\tau^*-\tau) \int_o^{\tau^*} J(t)\, E_2(\tau^*-t)\, dt \\
& + \frac{\omega_o(\tau)}{2} \mu_o\, r\, F\, E_2(\tau^*-\tau) \exp(-\tau^*/\mu_o) \qquad (5\text{-}15)
\end{aligned}
$$

where

$E_n(x) = {}_0\int^1 \exp(-x/\mu)\, \mu^{n-1} \frac{d\mu}{\mu}$ is the exponential integral

r is the wavelength dependent surface reflectance
$(0.0 \leq r \leq 1.0)$

Equation 5-15 must be solved for each wavelength, λ, of interest. The technique chosen to solve for the source function is the variational-iterative (VI) method developed by Sze (1976). The VI method is based on finding the extremum of a certain functional (hence the variational nature of the method). An a priori form of the unknown function (which is essentially the source function) is assumed, and the required coefficients are computed from a set of minimizing conditions. The form of the solution is specifically chosen to optimize computational efficiency and, therefore, accuracy is not sacrificed for speed. A comprehensive comparison between the simplest form of the VI technique (two-step functions) and the more common two-stream approximation (Chandrasekhm 1960) for a homogeneous, isotropic atmosphere has been conducted (Burke and Sze 1977). Results indicate that the VI technique is much more accurate for thin and moderate optical thickness ($\tau^* = 0.4$, 1.0, respectively), which characterize much of the 0.4 to 1.1 spectral region. For thicker atmospheres ($\tau^* \sim 3.5$), such as in the near-infrared water vapor bands, errors may be reduced to within a few percentages of the exact solution by iteration.

Once the source function $J(\tau)$ is found, the emergent intensity (that which would be measured by a sensor in space at wavelength, λ) is given by:

$$I(\lambda,\mu) = \int_0^{\tau^*} J(t) \exp\left[-\frac{(t-\tau)}{\mu}\right] \frac{dt}{\mu} \qquad (5\text{-}16)$$

where μ is the cosine of the zenith angle of observation.

However, as has been shown in Section 5.2, satellite sensors do not measure monochromatic radiation. On the contrary, they are most often sensitive to a finite bandwidth of wavelengths given by their respective spectral response functions, $\phi(\lambda)$. Therefore, the response-weighted radiances (the simulated instrumental values) are given by:

$$I(j,\mu) = \frac{\int_{\Delta\lambda} \phi_j(\lambda)\ I(\lambda,\mu)\ d\lambda}{\int_{\Delta\lambda} \phi_j\ (\lambda)\ d\lambda} \qquad (5\text{-}17)$$

where

$\phi_j(\lambda)$ is the spectral response function for the jth sensor/band

$\Delta\lambda$ are the wavelength limits of the sensor/band bandwidth

These functions for the DMSP VHR and Landsat MSS are given in Figures 2-1 and 2-3, respectively.

5.4.2 Results of Calculations

Radiative transfer calculations were performed for each of four model atmospheres previously described in Section 5.3. They are the basic tropical atmosphere with: (1) 23-km visual range, 80% relative humidity (3.35 g/cm^2); (2) 23-km visual range, 0.8% relative humidity (0.0335 g/cm^2); (3) 5-km visual range, 80% relative humidity; and (4) 5-km visual range, 0.8% relatively humidity.

The source function $J(\tau)$ was evaluated by applying the variational-iterative method to Equation 5-15 at each of 25 wavelengths within the 0.4 to 1.1 µm spectral interval. Wavelengths were selected to provide higher spectral resolution within the near-infrared region so that the structure of the water-vapor absorption bands would be apparent. Only five of the wavelengths were taken within the visible region where wavelength dependence is a smooth function. To solve for the source function, a profile of single scattering albedo versus optical depth, $\omega_0(\tau)$, was computed at each wavelength for each model atmosphere using spectral data from LOWTRAN 2 (Selby and McClatchey 1972). Sample single scattering albedo profiles are shown in Figure 5-7. At λ = 0.55 µm, the albedo is near unity for most of the atmosphere since scattering predominates as an extinction mechanism. At high altitudes (small τ), the albedo approaches lower values as absorption by the

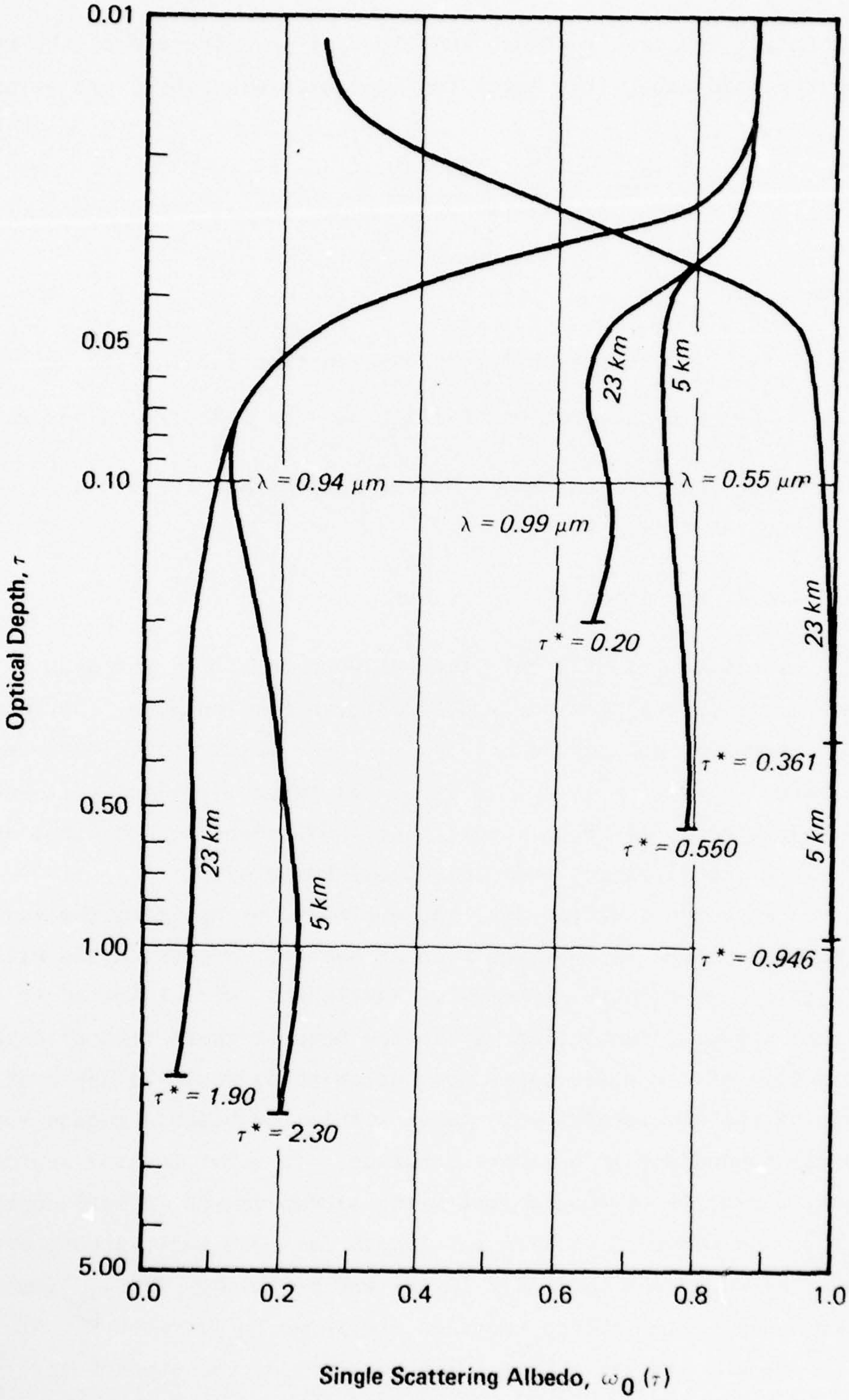

Figure 5-7 Single Scattering Albedo Profiles (Relative Humidity = 80%, Tropical Atmosphere)

Chappuis ozone bands becomes more important; however, the bulk of the atmosphere is purely scattering. The albedo profile takes on intermediate values at λ = 0.99 μm between two water vapor absorption bands where both scattering by aerosol and absorption by water vapor are evident. Higher in the atmosphere where both water vapor and aerosol are about, the albedo becomes unity owing to molecular scattering. At 0.94 μm, water vapor absorption is significant, and albedos are correspondingly low for much of the lower atmosphere. (Residual scattering from aerosol prevents it from becoming zero. Note the difference between the 5-km and 23-km visual range curves.)

The background surface is taken to be the sea surface, and a surface reflectance curve for water (Krinov 1947) is assumed. In general, the surface reflects about 5% of incident radiation in the visible and is black in the near infrared. Sun glint and other characteristics of a wind-driven waved surface are not considered. The solar elevation angle is assumed to be 45°. This value is a compromise between the mid-morning sun synchronous pass of the Landsat instrument and the characteristic early morning or mid-day DMSP vehicle. Since the emphasis here is on spectral differences, it was assumed that both sensors observe similarly illuminated scenes. For a more complete treatment, the relative geometries should also be considered. The observation angle for each sensor was taken to be slightly off nadir so that the results would be more characteristic of the bulk of pixels within a scan. The exact zenith angle is 25.8°.

Figure 5-8 illustrates the wavelength dependence of the normalized intensity before sensor response weighting. Plotted is $I(\lambda,\mu)/F$, where F is the incident solar flux at wavelength λ. Note that for a given relative humidity, the hazy atmosphere always appears brighter, even in the near-infrared water vapor absorption bands. However, for the more realistic case of correlated humidity and haze, a dry clear atmosphere may be brighter than a humid hazy atmosphere in strongly absorbing regions (see 0.94 μm).

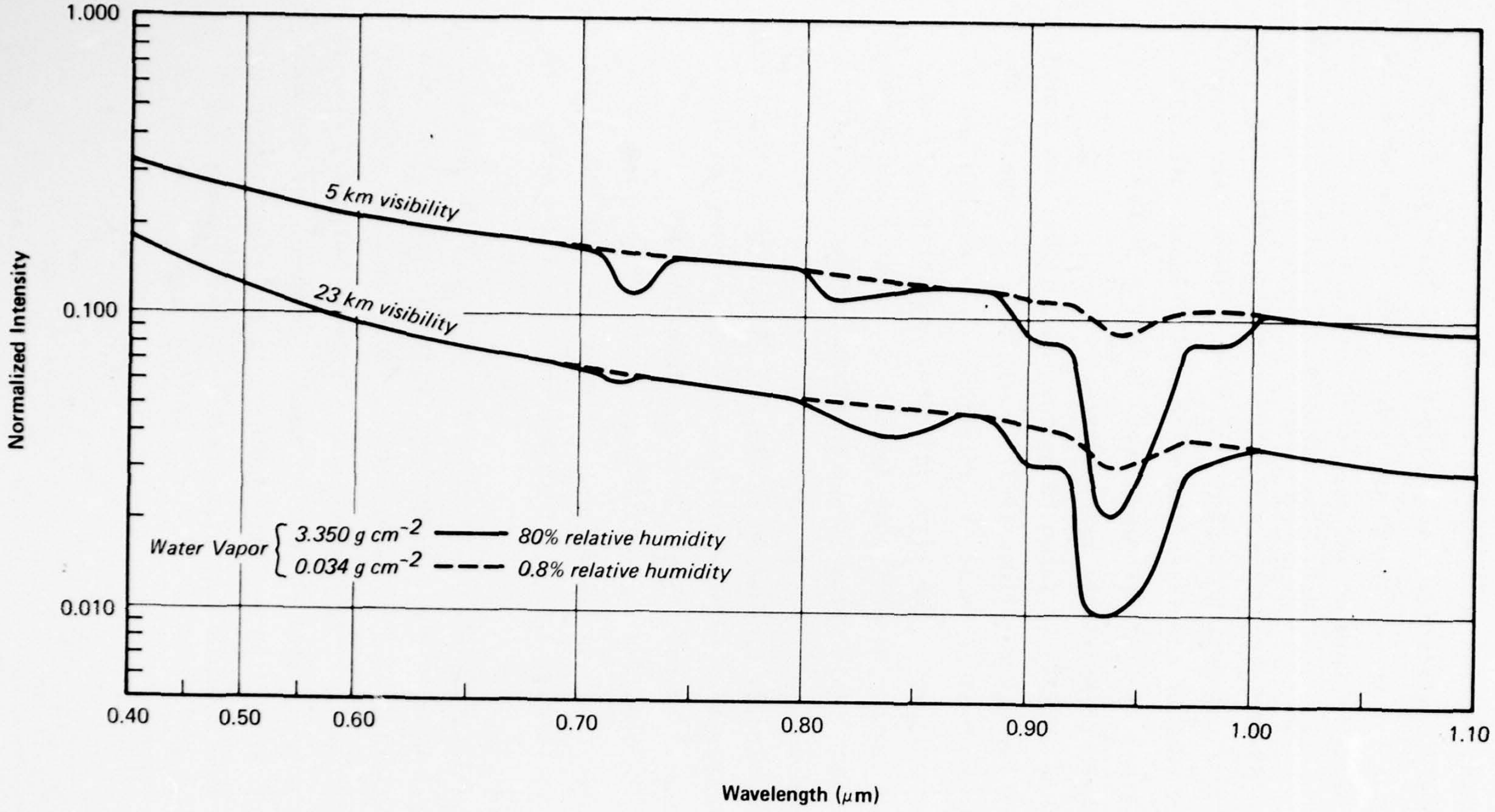

Figure 5-8 Simulated Radiance Spectrum (0.4 to 1.1 μm)

5.4.3 Response Weighted Radiances

Simulated satellite instrument radiances were computed by weighting monochromatic intensities with the appropriate spectral response functions for each instrument according to Equation 5-17. Results for the four model atmospheres are shown in Figure 5-9 for the Landsat MSS bands. For a given visibility (aerosol loading), only MSS-7 is sensitive to water vapor abundance. However, all bands are sensitive to aerosol content. For the cases considered, intensities decrease monotonically from MSS-4 through MSS-7. These calculations indicate that MSS-6 is most sensitive to changes in aerosol amount since Rayleigh scattering is minimal and water vapor is not a significant influence. However, the computed increased sensitivity in MSS-6 is not drastically greater than in MSS-4 or MSS-5.

The MSS-7 results must be carefully interpreted. The large difference between the 5-km visibility, low humidity radiance and the 23-km visibility, high humidity radiance is probably not physically realistic in light of the climatological correlation between high humidity and reduced visibility situations (Section 5.3). There, the hazy high humidity and clear low humidity results in MSS-7 should be compared. For the situation modeled, the results are comparable, suggesting that the effects of increased aerosol scattering and water vapor absorption compensate for one another. This conclusion will be case-specific, however, and requires careful consideration of an appropriate aerosol/humidity relationship.

Results for the DMSP instrument are given in Table 5-5, which includes the corresponding Landsat cases for comparison. In general, DMSP radiances are approximately the same as those in Landsat MSS-6. The effect of increased water vapor is to decrease DMSP radiances by about 5% to 8% (owing to absorption in the near infrared as evidenced by MSS-7 results). However, DMSP is most sensitive to aerosol content in these cases, increasing intensities by a factor of about 2.5.

The results shown in Table 5-5 may at first appear contrary to what would be expected since 45% of the contribution to the DMSP is from MSS-7 and only 25% from MSS-6 (see Figure 2-3). However, the response weighted radiances are not simply proportional to the relative

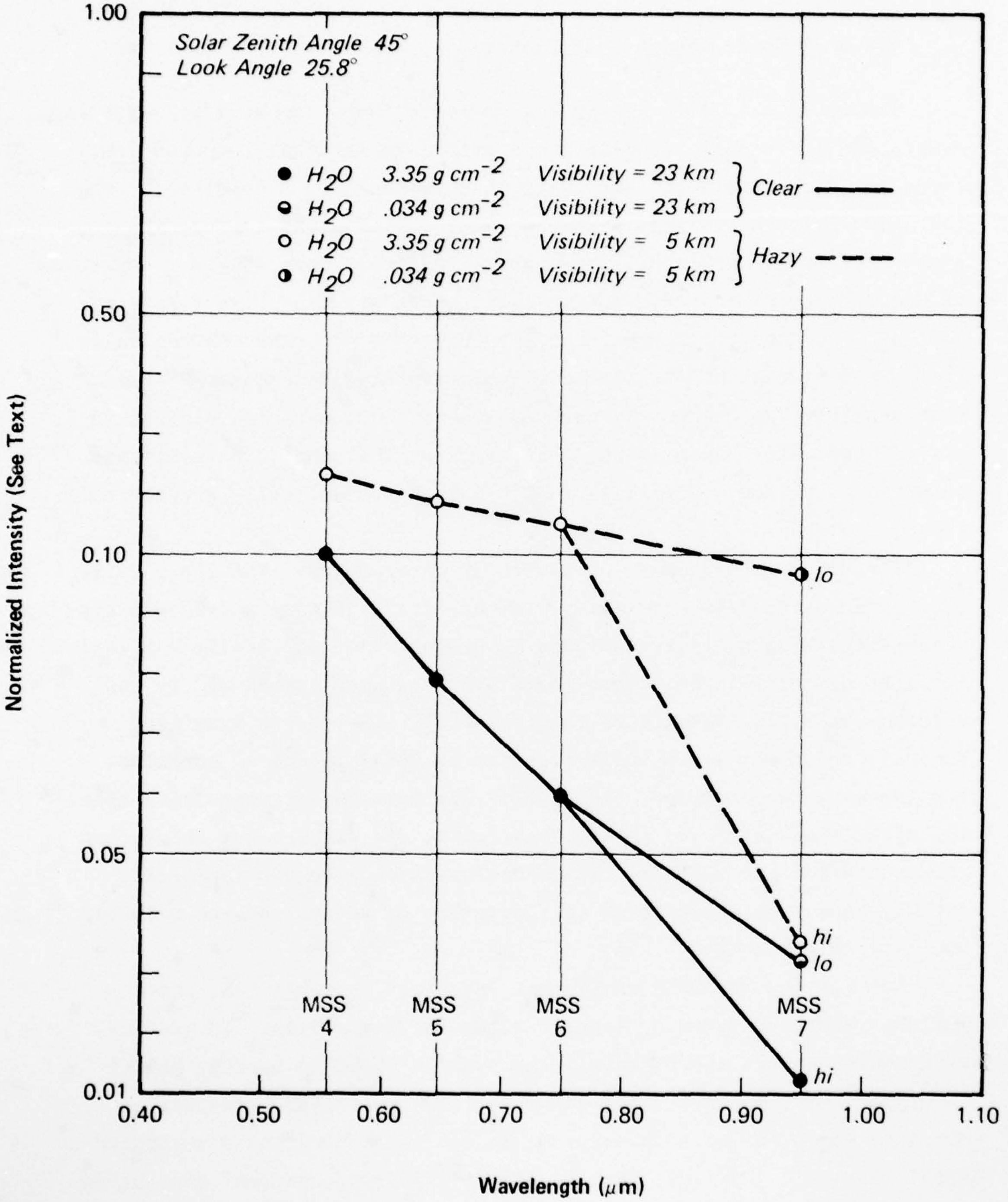

Figure 5-9 Landsat Normalized Intensities

TABLE 5-5

COMPARISON OF LANDSAT MSS AND DMSP BANDPASS WEIGHTED NORMALIZED INTENSITIES

	Visibility			
	23 km		5 km	
	Water Vapor (g/cm^{-2})			
Instrument	3.35	0.034	3.35	0.034
MSS-4	.105	.105	.234	.234
MSS-5	.080	.080	.194	.194
MSS-6*	.060	.060	.157	.157
MSS-7	.012	.033	.036	.097
DMSP	.059	.062	.146	.157

*The water vapor bands in Figure 5-8 near 0.73 μm have little effect on the MSS-6 bandpass weighted radiances and, so no change is shown with water vapor.

contributions from each spectral segment alone, but the product of relative contribution (based on response alone) times the radiance available. From Equation 5-17:

$$I(DMSP) \; = \; {}_{\Delta\lambda} \; \phi \;\; (\gamma) \; I(\lambda) \; d\lambda \; / \; {}_{\Delta\lambda} \; \phi(\lambda) \; d\lambda \qquad (5\text{-}18)$$

constructing the I(DMSP) from the Landsat bands alone, with the following percentages for each band (from Figure 5-5): MSS-4 10% ($\phi_4 = 0.10$); MSS-5 20% ($\phi_5 = 0.20$); MSS-6 25% ($\phi_6 = 0.25$); and MSS-7 45% ($\phi_7 = 0.45$).

The integral can be written as a sum:

$$I(DMSP) \; \simeq \; \sum_{i=4}^{7} \phi_i \; I_i \; / \; \sum_{i=4}^{7} \phi_i$$

where I_i are the Landsat MSS radiances given in Table 5-5 for each case.

Since $\sum_{i=4}^{7} \phi_i = 1.0$,

$$I(DMSP) \; = \; 0.10I_4 + 0.20I_5 + 0.25I_6 + 0.45I_7.$$

Using the radiances given in Table 5-5 for one case (Case 1: 23 km), as an example, the computed values are:

MSS	4	5	6	7	
$[\phi_i]$	0.10	0.20	0.25	0.45	$\sum\phi_i = 1.0$
$[I_i]$	0.105	0.080	0.060	0.012	
$[\phi_i I_i]$	0.0105	0.016	0.015	0.0054	$\sum\phi_i I_i = 0.047$ or I(DMSP) = 0.047

For this example case, it can be seen that although 45% of the DMSP response (ϕ_7) is covered by MSS-7, only 11.5% (.0054/.047) of the total DMSP energy is available at that wavelength. For the MSS-4, and wavelengths, the total energy available is 22.3%, 34.0%, and 31.9%, respectively. In fact, since energy available decreases towards MSS-7

(Figure 5-8), it is expected that although DMSP's response is 45% MSS-7, the higher energies available will systemmatically weight the lower MSS bands higher, and the integrated response will be characteristic of a lower band.

AD-A077 902 ENVIRONMENTAL RESEARCH AND TECHNOLOGY INC CONCORD MA F/G 4/2
COMPARATIVE STUDY OF ANOMALOUS GRAY-SHADE PATTERNS IN DMSP AND --ETC(U)
SEP 79 J C BARNES, C J BOWLEY, R G ISAACS N00228-77-C-3164
UNCLASSIFIED ERT-P-3469 NEPRF-CR-79-05 NL

2 OF 2
AD
A077902

END
DATE
FILMED
1-80
DDC

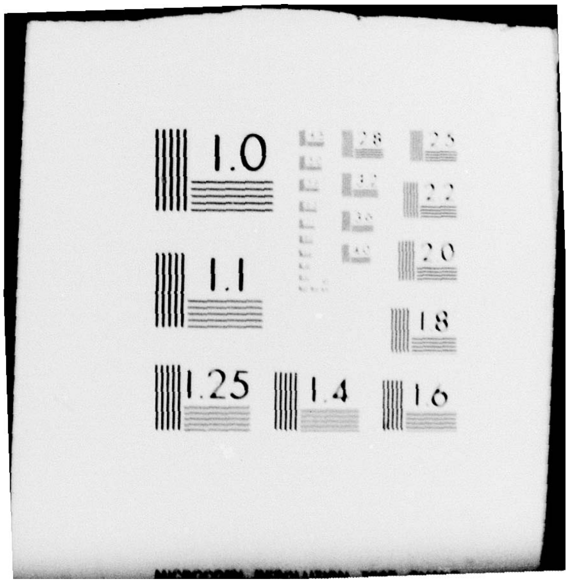
1.0
1.1
1.25
1.4
1.6
1.8
2.0
2.2
2.5
2.8
3.2
3.6
4.0

6. SUMMARY OF RESULTS

6.1 Comparative Analysis of DMSP and Landsat Imagery

The data sample used for the comparative analysis of DMSP and Landsat imagery was not as extensive as had been originally anticipated because of the difficulties encountered in finding cases with Landsat coverage in the area of an anomalous gray-shade pattern evident in a DMSP image. Landsat scenes only cover a very limited area, so in many potentially usable cases it was found that the Landsat coverage was just outside the DMSP anomalous gray-shade pattern. Moreover, several other potential cases were not usable because the only available DMSP data did not include the low- or log-enhancement images; anomalous gray-shade patterns cannot be detected except in the low- or log-enhancement data.

As a result of the difficulties in collecting a suitable data sample, most of the cases eventually selected for analysis were for land areas rather than the ocean. These cases satisfied the criteria of reduced visibility in light fog or haze and the Landsat observation being within two hours of the DMSP observation. However, the analysis of subtle gray-shade patterns in Landsat data is more difficult over land than over water because of the highly variable reflectance of the background at the Landsat 80-meter resolution. The results of the analysis of the cases described in Section 4 are summarized below.

6.1.1 Analysis of Cases Over Land

In all of the cases over land, the DMSP anomalous gray-shade pattern is in an area of high humidities and reduced visibilities. As explained in the theoretical discussion, high aerosol content (reduced visibilities) is likely to be associated with a moist atmosphere; the theoretical computations were based on this condition.

The results of the analysis indicate that in each case the Landsat MSS-4 (visible band) image displays an overall more hazy tone than the other spectral bands. In some cases where the Landsat scene is in the area of a relatively light-gray shade tone in the DMSP, the MSS-5 image also displays a somewhat hazy tone, although less than that of the MSS-4. In all cases, the MSS-6 and 7 (near infrared) images appear less hazy than the shorter wavelength bands; the MSS-6 generally appears somewhat hazier than the MSS-7. In the MSS-4 images, however, no distinct variation can be detected in the hazy tone from one portion of the image to another; rather, the images display an overall hazy tone even in areas where distinct tonal variations in the anomalous gray-shade pattern are evident in the corresponding DMSP image.

The hazy tone of the MSS-4 images can be established by examining the contrast between adjacent terrain features with high and low reflectivities. In Case 2 (Section 4.2), for example, it is readily evident that the contrast in the MSS-4 and 5 bands is considerably less than that in the MSS-6 and 7 bands. In at least one case, it was also possible to compare the contrast in MSS-4 images for a scene within a lighter tone area in the corresponding DMSP image and a scene within an area that appears darker in the DMSP; in this instance, the former image has a noticeably more hazy tone than the latter.

When comparing the various Landsat bands, it must be remembered that the contrast between water and vegetated land is much greater in the MSS-7 than in the MSS-4 band. In the near-infrared portion of the spectrum (MSS-7), water is essentially black whereas vegetation is highly reflective; in the visible portion of the spectrum (MSS-4), the difference in reflectance between water and land is considerably less. Because of the inherent greater contrast in the near infrared, it would be expected that a subtle haze pattern would be easier to detect in an MSS-4 image. Nevertheless, the results of the analysis cannot be attributed solely to this factor, and the observation that the MSS-4 band is consistently more hazy is in agreement with the findings of other investigators such as Fraser (1976) and Griggs (1978).

6.1.2 Analysis of Case Over Water

The case of an anomalous gray-shade pattern over water off the West Coast is quite different from the cases over land, where the patterns were associated with a synoptic pattern that produced a relatively broad area of high humidities and reduced visibilities. The anomalous gray-shade pattern off the coast appears to be associated with a more localized condition. The Landsat imagery indicates that the pattern seen in the DMSP is partly the result of small cloud cells that were below the resolution of the VHR sensor. However, since the DMSP pattern extends beyond the areas of the small cloud cells detectable in the Landsat imagery, it appears that the gray-shade pattern is also, in part, the result of an area of high moisture and high aerosol content remaining as the clouds dissipate; the remaining particles were even too small to be detected at the Landsat resolution. This finding is in agreement with the analysis of these particular DMSP images by Fett and Mitchell (1977).

In this case, the MSS-4 band appears to be measuring an overall higher radiance, although the pattern of cloud elements appears the same in the MSS-4, 5, or 6 bands; only in the MSS-7 band is the cloud pattern significantly reduced.

The comparative analysis for this case demonstrates the significance of the different resolutions of the DMSP VHR and the Landsat MSS. It may be, in fact, that the distinctive tonal differences observed within several of the anomalous gray-shade patterns in DMSP images are the result of the sensor integrating over a relatively broad area as compared to Landsat. When the image is produced, all of the individual picture elements within a certain reflectance value fall into a particular gray-shade tone that is distinct from the adjacent tone. The Landsat MSS, however, would detect several intermediate tones within the same area.

In the case over water, areas with low reflectance (black) can be detected along certain coastal areas in the Landsat imagery. These patterns, which are particularly pronounced in the MSS-5 band, are believed to be areas of calmer water within the lee of the land. Just south of the most pronounced of these black areas, a wave pattern in the water can also be detected, especially in the MSS-5 image.

6.2 Theoretical Analysis of Water Vapor Absorption

The theoretical analysis presented in Section 5 is based on certain assumptions: (a) a particular model atmosphere, water vapor amounts, and aerosol model and abundances; (b) a specific viewing geometry; (c) a simple radiative transfer model; and (d) viewing against a water surface.

Keeping these considerations in mind, the results of the theoretical analysis of the effects of water vapor on the satellite imagery indicate the following.

- DMSP and Landsat MSS-4, 5, and 6 radiances are more sensitive to aerosol scattering than to water vapor.
- Landsat MSS-7 radiances are highly sensitive to water vapor while DMSP is affected to a lesser degree.
- For realistic high humidity, low visibility situations, it is aerosol growth not water vapor, per se, which increases DMSP radiances; increased water vapor abundance, in fact, decreases radiances.
- Anomalous gray-shade patterns in areas where humidity is high are most likely the result of small aerosol droplets in the haze category (0.1 to 10 μm).
- Alternatively, when meteorological conditions are appropriate, anomalous gray-shade patterns may be caused by cloud droplets (20 to 400 μm), which are not yet organized into cloud elements large enough to be seen at the DMSP spatial resolution (1/3 nmi). In these cases, the observed anomalous gray-shade patterns in high humidity areas are caused more by the lack of spatial resolution of the DMSP instrument than by the lack of spectral resolution.

7. CONCLUSIONS AND RECOMMENDATIONS

7.1 Conclusions

A key requirement of the study was to compare DMSP and Landsat data to determine which wavelengths within the total DMSP spectral range are responsible for the anomalous gray-shade patterns. Under the scope of the effort it was possible only to carry out a comparative analysis of the satellite imagery; digital data were not analyzed. From the results of the imagery analysis, it is difficult to draw quantitative conclusions to address the question of which are the wavelengths most responsible for the observed DMSP response. The photographic processes used in producing the DMSP and Landsat images introduce substantial variability in the final products, whether on a day-to-day basis or even when the images for the different Landsat bands of the same scene are produced.

Furthermore, because of the limited data sample, only one case over a water background was analyzed. For the balance of the observed cases over land, specific conclusions are difficult to formulate since analysis of the imagery tends to focus on the "haziness" of the scene, which is really a measure of scene contrast reduction. An analysis of haziness would involve examining the changes in intensities for neighboring scene pixels with different surface reflectances (such as water vs. vegetation); calculations were performed, however, only for one surface type. Earlier analysis (Isaacs and Chang 1975) indicates that contrast reduction is very sensitive to spectral band pass, model atmosphere, and reflectance properties of the scene viewed.

The qualitative results of the imagery analysis indicate that the shorter wavelength Landsat bands, especially MSS-4, appear more hazy than the longer wavelength bands (MSS-6 and 7). The theoretical analysis, however, indicates that simulated radiances from the DMSP are similar to the Landsat MSS-6 band rather than to Band 4. As an explanation for this apparent contradiction, the relative contributions of energy from the different spectral intervals comprising the total DMSP response must be considered rather than the response function alone. Whereas only a 10% contribution at the MSS-4 wavelength might be expected from the response function, the relative energy contribution is actually more than 20%. The magnitude of the contribution at the MSS-4 wavelength, combined with the sensitivity of wavelengths near the peak DMSP response (0.7 to 0.8 μm) to increases in haze, results in the DMSP sensor being quite responsive to aerosol loading.

An alternative explanation for the apparent contradiction between the results of the imagery analysis and the theoretical analysis may be formulated based on the differing spatial resolutions of the two instruments (approximately 600 m for DMSP and 80 m for the Landsat MSS). With these resolutions, some 50 to 100 Landsat pixels are contained within one DMSP resolution element. Therefore, atmospheric features with continuously varying intensity responses, such as haze or developing clouds, are sampled by Landsat at a much higher resolution. The DMSP sensor, however, will produce an artificially distinct boundary since the varying intensities within the field-of-view will be averaged over a relatively broad area, as compared to Landsat. This explanation, related to the spatial resolutions of the sensor rather than to spectral differences, has not been investigated in the present study.

7.2 Recommendations for Further Study

The comparative analysis of the DMSP and Landsat imagery demonstrates the qualitative variation in intensities measured by the different spectral bands. In some cases, however, the variations in intensity are subtle and are difficult to assess fully through image analysis alone. It is recommended, therefore, that further analysis be carried out using Landsat digital tape data.

The analysis of digital tape data would permit a quantitative evaluation of the intensity variations. The contrast reduction over land could be determined, and variations in intensity over water that may not be detectable in the imagery could be measured. Furthermore, an experimental analysis of the Landsat data could be carried out to simulate the reduced resolution of the DMSP VHR. Such an analysis would determine whether the anomalous gray-shade patterns observed in the DMSP imagery are the result, at least in part, of the spatial averaging by the VHR sensor.

For further theoretical analysis, a study of realistic relative humidity/aerosol growth models is recommended to determine more accurately the water vapor and aerosol loading factors for the atmosphere. Such relationships, when included within the radiative transfer calculation, will enable the dynamics of aerosol growth pertinent to the asset and dissipation of reduced visibility situations as seen from space to be modeled.

It is also recommended that further analysis be undertaken to: (1) repeat the calculations carried out in this study substituting a maritime aerosol model and (2) evaluate the impact of aerosol scattering anisotropy on the model results. Under the first of these proposed additional tasks, the analysis would be extended by substituting a maritime aerosol model of Shettle and Fenn (1976). Optical properties of a model tropical atmosphere with varying water vapor amounts and the maritime aerosol amount would then be computed over the DMSP/Landsat spectral interval (0.4 to 1.1 μm), and radiative transfer theory would be used to evaluate monochromatic upward radiances using these optical properties. Finally, simulated satellite incident radiance would be calculated by weighting the monochromatic results using the appropriate DMSP and Landsat MSS sensor bandpasses.

Under the second task, calculations would be performed using an aerosol model with preferred scattering direction. Since Mie scattering is highly anisotropic, it is desirable to evaluate the magnitude of this effect on previous results. In this task two sample calculations would be made using a tropical atmosphere with maritime aerosol amounts and two diverse water vapor abundances. In addition to the optical properties available from the current study, the aerosol-scattering asymmetry factor would be evaluated using a computer code developed at ERT. The radiative transfer equation including scattering anisotropy would be solved, and both monochromatic and simulated DMSP/Landsat radiances would be computed. Results of the current study would be compared to assess the impact of anisotropy. It is expected that examination of the preferred scattering properties of the aerosol will lead to the delineation of specific sensor geometries favorable to the enhancement or suppression of anomalous gray shades.

REFERENCES

Ahlquist, N. C. and R. J. Charlson 1969. Measurement of the Wavelength Dependence of Atmospheric Extinction Due to Scatter. *Atmos. Env. 3*: 551-564.

Ångström, A. 1929. On the Atmospheric Transmission of Sun Radiation and on Dust in the Air. *Geogr. Annl. 12*:130.

Bowley, C. J., J. L. Horowitz, and J. C. Barnes 1977. *Analysis of Photochemical Oxidant and Particulate Pollution Pattern in New England Using Remote Sensing Data*. Final Report under Contract No. 68-02-2533 for EPA Region 1 Air Branch. Environmental Research & Technology, Inc., Concord, MA.

Burke, H. R. and N. D. Sze 1977. A Comparison of Variational and Discrete Ordinate Methods for Solving Radiative Transfer Problems. *J. Quant. Specrtosc. and Radiat. Transfer 17*:783-793.

Chandrasekhar, S. 1960. *Radiative Transfer*. Dover Publications.

Deirmendjian, D. 1964. Scattering and Polarization Properties of Water Clouds and Hazes in the Visible and Near Infrared. *Ap. Opt. 3*: 187-196.

Duntley, S. Q. 1948. The Reduction of Apparent Contrast by the Atmosphere. *J. Opt. Soc. Amer. 38*:179-191.

Feteris, P. J. et al. 1976. *Investigation of Mesoscale Cloud Features Viewed by Landsat*. Final Report under Contract NAS5-20804 for NASA/Goddard Space Flight Center. Environmental Research & Technology, Inc. Concord, MA.

Fett, R. W. and W. F. Mitchell 1977. *Navy Tactical Applications Guide: Vol. 1, Technique and Applications of Image Analysis (DMSP)*. NEPRF Applications Report 77-03. Tactical Applications Department, Naval Environmental Prediction Research Facility, Monterey, CA.

Fraser, R. S. 1976. Satellite Measurement of Mass of Sahara Dust in the Atmosphere. *Applied Optics 15*.10:2471-2479.

Goody, R. M. 1964. *Atmospheric Radiation*. London: Clarendon Press.

Griggs, M. 1978. *Determination of Aerosol Content in the Atmosphere from Landsat Data*. Final Report under Contract NAS5-20899 for NASA/Goddard Space Flight Center. Science Applications, Inc., La Jolla, CA.

Hidy, G. M. 1975. Summary of the California Aerosol Characterization Experiment. *J. Air. Poll. Contr. Assn. 25*.11:1106-1114.

Isaacs, R. G. and D. T. Chang 1975. *Experimental Evaluation of Atmospheric Effects of Radiometric Measurements Using the EREP of SKYLAB*. ERT Document No. P-410-F. Environmental Research & Technology, Inc. Concord, MA.

Kattawer, G. W. and G. N. Plass 1968. Influence of Particle Size Distribution on Reflected and Transmitted Light from Clouds. *Applied Opt. 7*:869-878.

Koschmieder, H. 1924. Theorie der Horizontalen Sichtweite. *Beitr. Phys. Atmos. 12*:171.

Krinov, E. L. 1947. Spectral Reflectance Properties of Natural Formations. *Laboratoriia Aerometodov*, Akad. Ivank. S.S.R, Moscow.

McClatchey, R. A. et al. 1973. *AFCRL Atmospheric Absorption Line Parameters Compilation*. AFCRL TR-73-0096. Air Force Cambridge Research Laboratories, Hanscom Field, Bedford, MA.

Middleton, W. E. K. 1958. *Vision Through the Atmosphere*. University of Toronto Press.

Mie, G. 1908. Beitrage Zur Optik Trueber Medien, Speziell Kolloidaker Metallosunger. *Annalen der Physik 25*:377-445.

Norwood, V. T., L. R. Fermelia, and G. A. Tadler 1972. *Multispectral Scanner System for ERTS: Four-Band Scanner System*. Final Report Vol. I. Report No. HS324-5214. Hughes Aircraft Co., El Segundo, CA.

Pueschel, R. F. and K. E. Noll 1967. Visibility and Aerosol Size Frequency Distribution. *J. Appl. Met 6*:1045-1052.

Selby, J. E. A. and R. A. McClatchey 1972. *Atmospheric Transmittance from 0.25 to 28.5 μm*. Computer Code LOWTRAN 2. AFCRL Environmental Research Papers No. 427, AFCRL 72-0745.

Shettle, E. P. and R. W. Fenn 1976. Models of the Atmospheric Aerosols and their Optical Properties. AGARD Conference Proceedings No. 183, *Optical Propagation in the Atmosphere*. Presented at Electromagnetic Wave Propagation Panel Symposium, Lyngby, Denmark, 27-31 October 1975. (NTIS Acc. No. N76-29817).

Sze, N. D. 1976. Variational Methods in Radiative Transfer. *J. Quant. Spectrosc. and Radiat. Transfer 16*:763-780.

van de Hulst, H. E. 1957. *Light Scattering of Small Particles*. New York: J. Wiley & Sons. pp. 13-14.

Willeke, K. and J. Brockman 1977. Extinction Coefficients for Multimodel Atmospheric Particle Size Distributions. *Atmos. Env. 11*:995-999.